AIChE

Deagglomeration of Nanoparticle Aggregates via Rapid Expansion of Supercritical or High-Pressure Suspensions

Daniel To and Rajesh Dave
Otto York Dept. of Chemical Engineering, New Jersey Institute of Technology, University Heights, Newark, NJ 07102-1982

Xiaolong Yin and Sankaran Sundaresan
Dept. of Chemical Engineering, Princeton University, Princeton, NJ 08544

DOI 10.1002/aic.11887
Published online August 19, 2009 in Wiley InterScience (www.interscience.wiley.com).

Deagglomeration of suspensions of alumina and titania nanopowders (i.e., nanoparticle aggregates) via rapid expansion of supercritical suspensions (RESS) or high-pressure suspensions (REHPS) was studied. The size distribution of fragmented nanopowders was characterized by online Scanning Mobility Particle Spectrometer (SMPS) and Aerodynamic Particle Sizer (APS), and by offline Scanning Electron Microscopy (SEM). SMPS and SEM measurements indicate that the average agglomerate sizes were well below 1 μm, consistent with the length scales observed in our complementary RESS/REHPS mixing experiments using alumina and silica nanopowders. The APS measurements, on the other hand, were affected by reagglomeration during sampling and yielded an agglomerate size range of 1 to 3 μm. Analysis of the RESS/REHPS process through compressible flow models revealed that both the shear stress in the nozzle and the subsequent impact of the agglomerates with the Mach disc in the free expansion region can lead to micron or sub-micron level deagglomeration. © 2009 American Institute of Chemical Engineers *AIChE J,* 55: 2807–2826, 2009
Keywords: deagglomeration of nanoparticle agglomerates, characterization of nanoparticle agglomerates, supercritical fluids, rapid expansion, nanoscale mixing

Introduction

Nanoparticles and nanocomposite materials have many unique properties owing to their small particle/grain size and large contact area between the nanosized constituents.[1–3] A major challenge in making and handling such materials is the tendency of the nanoparticles to aggregate due to van der Waal forces and form large fractal structures in tens or hundreds of microns in size.[4–8] Composite materials made by simply mixing agglomerates of the constituent nanoparticles will invariably have much smaller contact area between constituents than is theoretically possible and will therefore lack the potential advantages that nanocomposites can offer. The full potential of a nanocomposite material can only be achieved when the constituent nanoparticles are properly dispersed and mixed—preferably at a nanoscale—and the agglomeration between particles is well controlled. Unfortunately, conventional methods for powder mixing tend to be homogeneous only above the scale of tens of microns because they fail to break the primary aggregates.[9–12] There

Correspondence concerning this article should be addressed to R. Dave at dave@adm.njit.edu

is a need for innovative approaches to achieve efficient nanoscale deagglomeration and mixing,[13–17] as well as elucidation of the various deagglomeration mechanisms.

In addition to mixing, deagglomeration of nanopowders can also be desirable in other contexts such as controlling the light scattering efficiency,[18] the suspension viscosity,[19,20] and the bulk density of materials.[21–23] For example, several researchers have found that reducing agglomerate size led to an increase in the relative density (ratio of compact bulk density to the true density) of dry powder compacts, which upon sintering led to improved bulk properties and product uniformity.[19–21]

Nanoparticle agglomerates are commonly broken down and dispersed using a variety of wet methods that use either high shear or ultrasonic cavitation, in conjunction with organic solvents, surfactant, or pH modifiers.[19,20,24–27] High-shear devices employ viscous drag and eddy formation to break nanoparticle agglomerates. Examples include high-pressure homogenization (throttling a liquid suspension through a fine capillary nozzle) or high-speed/high-shear stirring. Using a motionless high-pressure homogenizer for individual suspensions of zirconia (12 nm), silica (7, 12, 20, and 30 nm), and titania (21 nm) in an ethylene glycol aqueous solution. Seekkuarchchi and Kumazawa[19] showed that nanoparticle agglomerates could be broken down below 100 nm. Ultrasonic devices, on the other hand, focus acoustic energy to very small length scales to produce cavitation, microjets, and large pressure gradients[24] to facilitate deagglomeration.[20] Although wet methods are effective means to produce stable suspensions of mixed and deagglomerated nanopowders, they require the use of organic (or aqueous) solvents, surfactants, or other interfacial agents; furthermore, producing dry powder from suspensions is often a slow and energy-intensive process in which many difficult issues may arise, such as density based stratification and electrostatic separations during drying. Therefore, there is a need for simpler approaches for deagglomeration and mixing of nanopowders that minimize the use of environmentally hazardous solvents, surface agents, and suspensions.

In recent years, many environmentally benign dry methods have been proposed and investigated to mix nanopowders for the purpose of obtaining composite products.[5,13–17,28,29] These methods include: mixing by Rapid Expansion of Supercritical Suspensions or High-Pressure Suspensions (RESS/REHPS),[13–15,17] mixing by stirring in supercritical fluids,[13–15,17] Magnetically Assisted Impaction Mixing (MAIM),[15,16] mixing via sonication in supercritical fluids,[28] and mixing by fluidization of nanopowders.[5,15,29] In the RESS/REHPS process, insoluble nanopowders are stirred and then expanded through a fine capillary nozzle. It was concluded in previous studies[13,14] that a high degree of mixing occurred due to the rapid expansion of the suspension and not because of simply stirring in supercritical carbon dioxide prior to the expansion. These mixing experiments offer indirect proof that effective deagglomeration of the original agglomerates has taken place in the RESS/REHPS process. In the present study, we characterize through various means the agglomerate fragments produced via RESS/REHPS and demonstrate that this process is indeed an effective means for deagglomeration of nanopowders. Major advantages of RESS/REHPS process are; no need for drying, the process is environmentally benign, and it is a potentially scalable process as evidenced by large-scale equipment available for a similar process, namely, SCF based extraction.

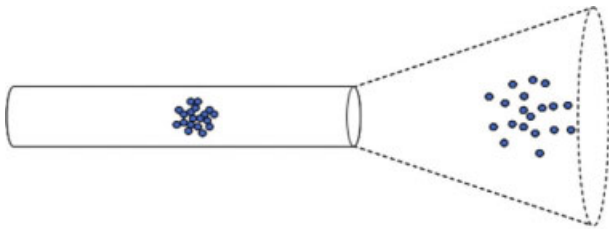

Figure 1. Schematic representing RESS deagglomeration.

[Color figure can be viewed in the online issue, which is available at www.interscience.wiley.com.]

Deagglomeration of cohesive powders via rapid depressurization has been the subject of several other investigations.[30–33] These studies have generally looked at the deagglomeration of particles whose size is in the range of 1–50 microns. Weimer et al.[32] showed that the conversion of 15-micron Al particles to AlN reached almost 90% when the particles were completely deagglomerated, as opposed to 49% when the particles were in the form of aggregates. Kobayashi[33] showed that the equivalent diffusion coefficient of SO_2 to agglomerated limestone powders, generally a size independent parameter, increased with increasing limestone agglomerate sizes due to the inability of SO_2 in penetrating the aggregate structure. However, to date, systematic investigation of rapid expansion of agglomerates that contain nanosized primary particles has not been reported.

In RESS/REHPS, the high shear stress in the nozzle can cause deagglomeration; furthermore, passing through the Mach disc in the freely expanding jet, if formed, can be another means for agglomerate breakup. Brandt et al.[34] investigated the effect of shock waves on deagglomeration of nanopowder agglomerates in a shock-tube filled with argon. Two types of nanopowders, Degussa Aerosil OX50 and Aerosil TT600 (both silica powders, $d_p = 40$ nm, but with different bonding surface energy levels), were studied and the agglomerate sizes were measured by in situ laser scattering. It was observed that as the agglomerates passed through the shock, their (count mean) diameters were reduced to about 200 nm for OX50 and about 400 nm for TT600.

In our study, deagglomeration of nanopowders by RESS/REHPS has been investigated via experiments and modeling of the rapid expansion process, which is described in Figure 1. Our experimental RESS/REHPS system, which will be introduced in more detail in the next section, closely resembles the well-known RESS process used mainly for rapid precipitation of solutes to form very fine powders (refer recent review articles[35–39]). Our deagglomeration experiments involved two different types of nanoparticle agglomerates (alumina and titania), and were carried out under several different operating conditions. The resulting particle size distributions were characterized using multiple experimental techniques. These experiments were complemented by modeling of the rapid expansion process[40–46] to elucidate the deagglomeration mechanisms. Through modeling, we were able to assess the relative importance of deagglomeration through shear in the nozzle

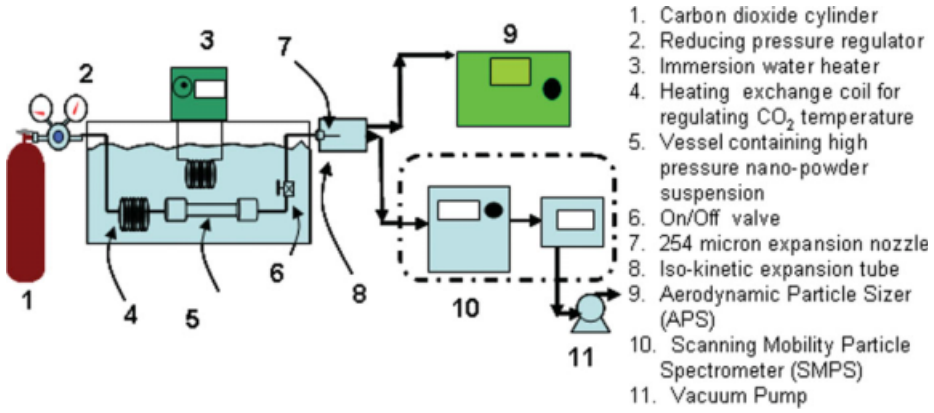

Figure 2. Schematic of RESS apparatus and online characterization equipment.

[Color figure can be viewed in the online issue, which is available at www.interscience.wiley.com.]

and via impaction at the Mach disc, including how they were influenced by the operating conditions.

Experimental Setup

Figure 2 shows a schematic of our experimental system. About 0.1 g of the powder sample to be deagglomerated, alumina Alu C ($d_p = 13$ nm) or titania P25 ($d_p = 21$ nm) supplied by Evonik Degussa GmbH, was charged into a 24 ml tubular mixing vessel (unit 5 in the Figure 2) (supplied by High Pressure Equipment) and suspended in supercritical or high-pressure carbon dioxide (99.9% pure, supplied by Welco Gas). The pressure inside the mixing vessel was controlled by a one-stage pressure-reducing regulator (unit 2; Matheson Tri-gas) and was varied between 1.72 and 7.93 MPa in this work. The temperature of the CO_2 supply was raised to 45°C when it passed through a 2 m (length) × 0.762 mm (ID) stainless steel coil heat exchanger (unit 4), immersed in a water bath equipped with a heating coil (unit 3). The mixing vessel was also immersed in the water bath to maintain its temperature. The RESS experiment was initiated by opening the on/off valve (unit 6) and allowing the supercritical/high-pressure CO_2 containing the suspended nanoparticle agglomerates to expand through a capillary nozzle [10 cm (length) × 254 micron (ID); unit 7]. The expanded CO_2 stream was then directed into a 26.7 cm (length) expansion tube (unit 8). Expansion tubes of different diameters were used for different upstream pressures to ensure that the linear velocity of the suspension upon exiting the expansion tube was roughly constant (3.2 m/s) to facilitate iso-kinetic sampling for size distribution determination. The inner surface of the expansion tube was coated with vacuum grease to ensure that agglomerates that collide with the tube will mostly be trapped, thus mitigating their interference with the measurements.

The size distribution of fragmented nanopowders in the form of aerosols was characterized by two online techniques: differential mobility analysis and aerodynamic time-of-flight analysis. A Scanning Mobility Particle Spectrometer (SMPS, Model 3080; unit 10) and an Aerodynamic Particle Sizer (APS, Model 3321; unit 9) (both made by TSI) were used to perform these analyses, respectively. An additional off-line technique involved imaging the agglomerates using a field emission scanning electron microscope (SEM, LEO 1530VP), followed by image analysis using ImageJ®, a public domain software, to determine the projected-area-equivalent-diameter of the agglomerates.

The SMPS uses the different mobilities of the agglomerates to determine their sizes and determine the size distribution; our SMPS unit is rated to measure particle sizes in the range of 19 to 572.5 nm. The expanded aerosol suspension was drawn into the SMPS at 0.27 l/min through a 60 cm long, 0.64 cm, ID hose. The sheath air was set at 2.7 l/min to achieve the optimum sheath flow to aerosol flow ratio of 10 to 1. Two correction algorithms offered by the SMPS were applied to account for potential errors: the Diffusion Loss Correction was applied to account for the loss of agglomerates below 100 nm within the SMPS, and the Multiple Charge Correction prevents undersizing due to the occurrence of multiple charges on agglomerates larger than 100 nm.

The SMPS can be operated in either (A) a non-scanning mode that monitors the concentration of agglomerates of a chosen diameter as a function of time, or (B) a scanning mode that determines the size distribution by scanning over a range of diameters. The data presented here were obtained using the scanning mode. As a scan typically requires 60 s, it was necessary to ensure that during this time the concentration of aerosols for each size was roughly constant. Therefore, we performed a number of RESS experiments employing the non-scanning mode of the SMPS to examine how aerosol concentration changed with time at various chosen diameters. These experiments revealed that concentrations became nearly steady between 90 and 300 s after the initiation of the RESS experiment. Therefore, when we used the scanning mode of the SMPS to determine the size distribution, we began gathering data 100 s after initiating the RESS experiment; three successive measurements were made for each experiment and each of them lasted 60 s: 100–160, 160–220, and 220–280 s. The experiment was repeated three times, thus generating nine size distribution data sets for each operating condition. We also conducted REHPS experiments using compressed nitrogen at 1.72 and 7.93 MPa (and alumina nanopowders) to examine the possibility of using

other gases for deagglomeration. In those experiments, we used SMPS and followed similar steps to determine the agglomerate size distributions.

The APS is rated to measure particle sizes in the range of 0.5 to 20.0 μm. The aerosol suspension from the expansion chamber was drawn through a hose (0.64 cm ID, 60 cm long) and delivered to the detector at a flowrate of 1 l/min. Additionally, sheath air was drawn in at 4 l/min. Data were also recorded at the same time windows as in the SMPS measurements (100–160, 160–220, and 220–280 s) and the experiments were repeated in triplicate to produce a total of nine size distribution data sets for each operating condition.

We also used an off-line method based on Scanning Electron Microscopy (SEM) to determine the size of the agglomerates after the expansion. When we collected agglomerate samples to perform SEM analysis, we only used units 1–7 of the RESS apparatus (c.f., Figure 2). Samples of agglomerates were collected from the expanded aerosol stream by Brownian diffusion on a smooth silicon chip mounted on a 13 mm aluminum stub. The chip was placed at the centerline of the stream, 6 inches away from the exit of the nozzle, and the surface of the chip was held parallel to the direction of the aerosol flow, minimizing its influence on the aerosol stream. This parallel configuration of the collecting surface also reduced the possibility of agglomerate fragmentation due to collisions between the agglomerates and the surface. The SEM images of the agglomerates were analyzed using ImageJ®, where a brightness threshold was set to convert the SEM images into binary images, making the background (chip surface) white and the foreground (agglomerates) black. The characteristic size of the agglomerate was calculated as the diameter of a circle enclosing the same projected area as the agglomerate. In general, ~1000 agglomerates were sized using this method for each experiment.

Although the rapid expansion process is expected to fragment the aggregates of nanoparticles, these fragments are likely to undergo some degree of reagglomeration in the expansion tube and in the hose that connects the expansion tube to the online measurement devices; thus, these measurements do not necessarily yield the size distribution of the agglomerates prior to reagglomeration. To achieve a better assessment of the performance of our RESS/REHPS system in deagglomeration, we performed a small number of mixing experiments where Alumina Alu C and silane coated silica R972 ($d_p = 16$ nm), the mole fractions of which were chosen to be at mullite ($3Al_2O_3{\cdot}2SiO_2$) stoichiometry, were loaded into the mixing chamber, mixed manually by shaking, and then processed by RESS/REHPS. In the mixing experiments, the pressure of the mixing vessel was maintained at 7.93 MPa, and the powders were collected on a 0.22 micron Millipore filter. The collected powders were then pressed at 600 MPa into 13 mm tablets. The quality of the mixture was characterized by SEM in conjunction with energy dispersive x-ray spectroscopy (EDS) to determine the concentrations of alumina and silica at various spatial locations.

Experimental Results on Deagglomeration

The SMPS, APS, and SEM imaging were used to characterize the sizes of the agglomerates after expansion from different mixing chamber pressures. Each experiment was performed in triplicate, with three sets of data per experiment as explained earlier. The nine data sets were averaged to determine size distribution statistics. In this manner, the number- and volume-weighted mode diameters were obtained for each mixing vessel pressure P_0. In what follows, the size distributions are reported as relative number frequency, χ_n, and relative volume frequency, χ_v, as functions of diameter.

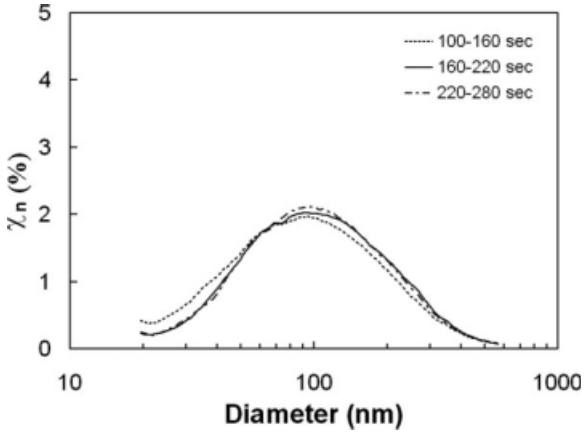

Figure 3. Number-weighted distributions of alumina nanopowders expanded from 5.86 MPa through a 254 μm × 10 cm nozzle; extracted from SMPS measurements taken at three successive time windows: 100–160, 160–220, and 220–280 s.

$$\chi_{n,i} = n_i \Big/ \sum_j n_j \qquad \chi_{v,i} = n_i\, v_i \Big/ \sum_j n_j v_j \qquad (1)$$

Here, n_i and v_i denote the number of occurrences and volume of agglomerates whose diameters lie in the region d_i and $d_i + \Delta d_i$, where Δd_i is the diameter window used to classify the agglomerate size data. It is understood that diameter henceforth refers to mobility diameter (SMPS), aerodynamic diameter (APS), or projected area diameter (SEM).

SMPS size analysis

As mentioned earlier, for each experiment, we collected size distribution data sets over three time windows: 100–160 s, 160–220 s, and 220–280 s after initiating the experiment. Figure 3 shows a typical measurement: the three size distributions obtained by the SMPS over the three time windows are very similar, indicating that there is no significant change in the agglomerate size distribution over time from 100 to 280 s.

Although not shown, similar control experiments were performed where only carbon dioxide was expanded through the nozzle. At the lower mixing vessel pressures of 1.72 to 5.86 MPa, the SMPS did not detect any particles, suggesting that there was neither condensation of CO_2, nor condensation of potential dissolved impurities. At the highest pressure (7.93 MPa), small amount of aerosol particles were detected at times greater than 220 s from the initiation of the

Table 1. Number- and Volume-Weighted Mode Mobility Diameters and Standard Deviations for Alumina and Titania Nanopowders Expanded Through a 254 μm ID × 10 cm long nozzle

	Alumina				Titania			
	Number Weighted (nm)		Volume Weighted (nm)		Number Weighted (nm)		Volume Weighted (nm)	
Pressure (MPa)	Mode	SD	Mode	SD	Mode	SD	Mode	SD
1.72	85/71	89/85	532/266	136/112	79	80	>572.5	139
3.79	69	95	372	132	69	80	346	132
5.86	91	86	346	131	62	78	358	133
7.93	35/66	89/105	346/219	129/116	37	72	260	122

These values correspond to the distributions shown in Figures 4 and 5. In the entries for alumina powders, the numbers after the slashes were obtained using N_2 as the working medium instead of CO_2.

experiment. These particles, assumed to be dry ice, were at a concentration of about 10^5 counts/cm^3 and a mode size below 25 nm. This concentration is one to two orders of magnitude smaller than the counts obtained in the deagglomeration experiments, indicating that condensation of CO_2, even at the highest pressure of 7.93 MPa, does not interfere significantly with the measurements of agglomerate size distribution.

The number- and volume-weighted mode diameters of expanded alumina and titania measured by the SMPS, listed in Table 1, show that the nanopowders were significantly deagglomerated by the RESS/REHPS process. The corresponding size distributions are shown in Figures 4a, b and 5a, b. The number-weighted mode diameters were all below 100 nm. The measured size distributions were all very wide (the standard deviations are significant when compared to the mode diameters). For alumina powders, there was no clear trend indicating whether the agglomerate size increased or decreased with pressure at the lower pressures (1.72–5.86 MPa); for titania powders, the agglomerate size appeared to decrease with increasing pressure, but the dependence was weak. It was only at the highest pressure that a significant reduction in the number-weighted mode diameters was observed. The volume-weighted mode diameters decreased with increasing pressure. However, the fact that some of the volume-weighted mode diameters were close to the SMPS measurement upper limit of 572.5 nm indicated that agglomerates larger than 572.5 nm were likely to be present. The trend observed in the REHPS experiments using nitrogen as the suspending medium was similar: when the pressure decreased from 7.93 to 1.72 MPa, the number-weighted agglomerate size increased from 66 nm to 71 nm, and the volume-weighted agglomerate size increased from 219 nm to 288 nm.

APS size analysis

The APS measured the time required for an agglomerate to pass a distance of ninety microns to calculate its velocity, from which the aerodynamic diameter of the agglomerate was determined. Classically, the aerodynamic diameter should be calculated based on results obtained in a stagnant gas. When determined in the presence of gas flow (outside of the Stoke regime, $N_{Re} > 0.5$) it can be affected by the agglomerate density. The APS uses a recursive algorithm referred to as the Stokes correction[47] to determine the corrected aerodynamic diameter D_{a2} from the measured diameter D_{a1}, the gas density ρ_a, gas viscosity μ, the relative velocity of the agglomerate to the gas flow ($U - \overline{V}$), the true agglomerate density ρ_2 and a calibration standard with a density of ρ_1 (1000 kg/m^3):

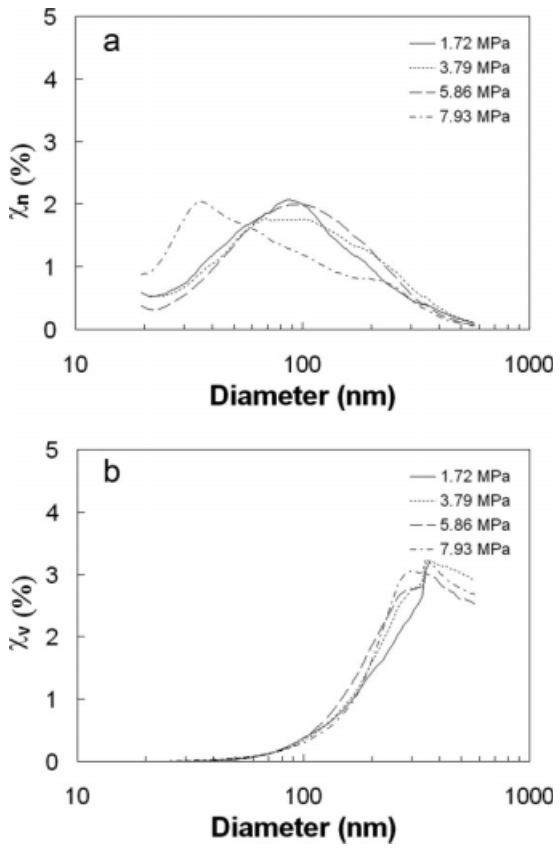

Figure 4. a: Number-weighted distributions of alumina nanopowders expanded from various pressures through a 254 μm × 10 cm nozzle; obtained by averaging the data obtained over several SMPS measurements. b: Volume-weighted distributions of alumina nanopowders expanded from various pressures through a 254 μm × 10 cm nozzle; obtained by averaging the data obtained over several SMPS measurements.

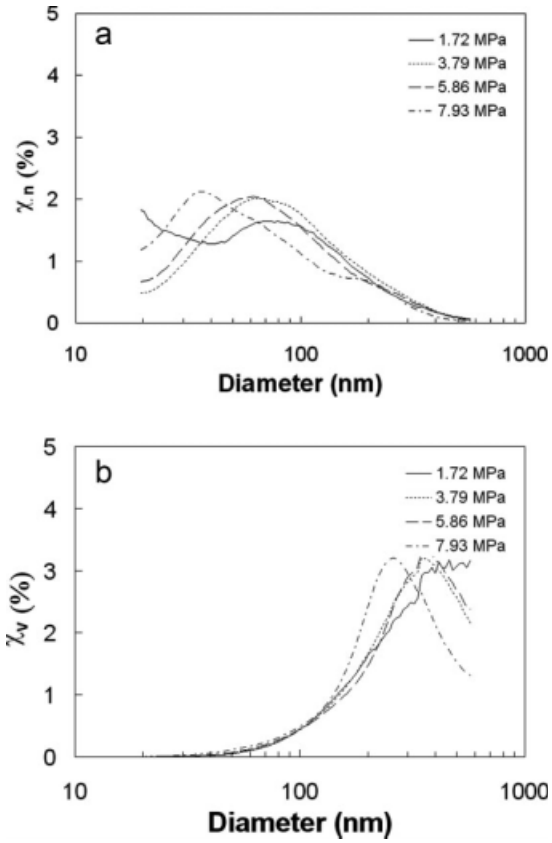

Figure 5. a: Number-weighted distributions of titania nanopowders expanded from various pressures through a 254 μm × 10 cm nozzle; obtained by averaging the data obtained over several SMPS measurements. b: Volume-weighted distributions of titania nanopowders expanded from various pressures through a 254 μm × 10 cm nozzle; obtained by averaging the data obtained over several SMPS measurements.

$$D_{a2} = D_{a1}\left[\frac{6+R_2^{2/3}}{6+R_1^{2/3}}\right]^{1/2}; \quad R_1 = \frac{\rho_a(U-\bar{V})D_{a1}}{\mu\sqrt{\rho_1}}; \quad R_2 = \frac{\rho_a(U-\bar{V})D_{a2}}{\mu\sqrt{\rho_2}} \tag{2}$$

Because of the Stokes correction, the density for the agglomerate affects the estimate of the aerodynamic diameter. Our system is further complicated by the fractal nature of the agglomerates, resulting in size-dependent agglomerate density. The fractal pattern, which follows a quasi-power-law equation, relates the number of particles in an agglomerate, N, to the ratio of the diameters of the agglomerate and the primary particle, (L_{agg}/L_p):

$$N = k\left[\frac{L_{agg}}{L_p}\right]^{D_f} \tag{3}$$

where k is a constant and D_f is the fractal dimension. It then follows that the agglomerate density is given by

$$\rho_{app} \approx \rho_{true}\left[\frac{L_{agg}}{L_p}\right]^{D_f-3} \tag{4}$$

Agglomerates of nanoparticles tend to have fractal dimensions close to 2.5 corresponding to the diffusion-limited aggregation case.[4,5,48] Although the fractal dimension is often treated as a constant independent of the agglomerate size, it has been shown that the agglomerates composed of natural kaolinite particles were better represented by a variable fractal dimension.[49–51] Such variable fractal dimension would further complicate the estimate for agglomerate density. As information on the variation of the agglomerate density with agglomerate size is unavailable for our powders, definitive Stokes correction is not possible. Consequently, we tested the influence of different choices for the agglomerate density on the corrected aerodynamic diameter distribution extracted from the APS data. Figures 6a, b show the number- and volume-weighted distributions obtained in one

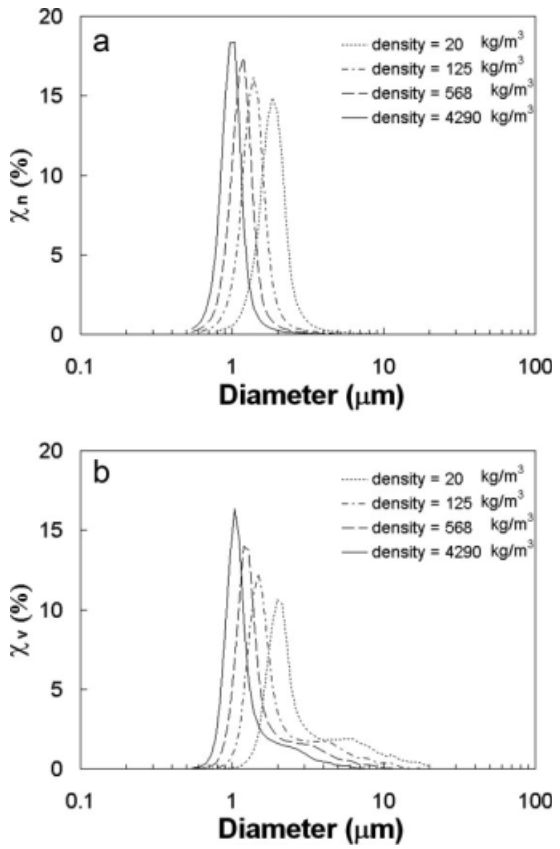

Figure 6. a: Number-weighted distributions of titania nanopowders expanded from 5.86 MPa through a 254 μm × 10 cm nozzle; extracted from APS measurements. The Stokes correction of size is based on assumed densities of 4290, 568, 125, 20 kg/m^3. b: Volume-weighted distributions of titania nanopowders expanded from 5.86 MPa through a 254 μm × 10 cm nozzle; extracted from APS measurements. The Stokes correction of size is based on assumed densities of 4290, 568, 125, 20 kg/m^3.

Table 2. Number- and Volume-Weighted Mode Geometric Diameters and Standard Deviations for Alumina and Titania Nanopowders Expanded Through a 254 μm ID × 10 cm long nozzle

	Alumina				Titania			
	Number Weighted (μm)		Volume Weighted (μm)		Number Weighted (μm)		Volume Weighted (μm)	
Pressure (MPa)	Mode	SD	Mode	SD	Mode	SD	Mode	SD
1.72	1.98	0.77	1.98	3.59	1.49	0.41	1.60	2.02
3.79	1.84	0.68	2.13	2.77	1.49	0.44	1.60	2.51
5.86	1.98	0.91	2.13	2.68	1.49	0.44	1.60	2.39
7.93	1.98	0.77	2.13	3.03	1.49	0.61	1.60	3.86

These values correspond to the distributions shown in Figures 7 and 8.

experiment involving titania powder for various assumed values of the density. Included are the results for true density (4290 kg/m^3), the bulk density of the agglomerate sample as obtained (125 kg/m^3), the density at the mode agglomerate size assuming a fractal dimension of 2.5 (568 kg/m^3), and the density at the mode agglomerate size assuming a fractal dimension of 1.8 (20 kg/m^3). It is clear from Figures 6a, b that the size distributions become wider, with the mode diameter increasing with decreasing agglomerate density. It should be noted that even though the density was varied over two orders of magnitude, the number- and volume-weighted mode diameters were relatively stable: the number-weighted mode diameter varied between 0.97 and 1.84 microns, and the volume-weighted mode diameter varied between 1.04 and 1.98 microns. Thus, the uncertainty in agglomerate density does not affect the typical order of magnitude of APS size measurements. In what follows, we have assumed in the APS analysis that the agglomerate densities were the same as their respective bulk densities (125 kg/m^3 for titania and 48 kg/m^3 for alumina).

The number- and volume-weighted mode diameters of the expanded alumina and titania nanopowders, measured by the APS, are listed in Table 2. The measured mode diameters were nearly independent of the variation in pressure as shown in Figures 7 and 8. The number- and volume-weighted mode diameters were similar, suggesting that the size distributions were relatively narrow. Indeed, Figures 7 and 8 indicate that the vast majority of the agglomerates had diameters between 1 and 3 microns.

The agglomerate size data listed in Tables 1 and 2 are very different—this is expected because SMPS and APS cover different size ranges, with practically no overlap. If the agglomerates entering SMPS/APS had a narrow, unimodal size distribution, then either SMPS or APS would detect a peak, but not both. The fact that both SMPS and APS measurements detected peaks in their respective sizing ranges suggests that: (a) The size distribution of the agglomerates was wide and not unimodal, and/or (b) reagglomeration might have occurred in the expansion tube and the hose leading to SMPS/APS units, producing large agglomerates that were detected by the APS. We expect that reagglomeration would not affect the SMPS very much, because the large agglomerates formed by reagglomeration would fall out of the sizing range of the SMPS. Through the mixing experiments, the detail of which will be discussed later in the article, we confirmed that the larger agglomerates detected by the APS indeed came from reagglomeration after the expansion, and that the sizes reported by the SMPS were more indicative of the actual sizes of the agglomerates immediately after the expansion.

Diffusion collection and SEM image analysis

The number- and volume-weighted mode diameters of the agglomerates collected on the surface of silicon chips, measured by SEM imaging, are listed in Table 3. Typical images

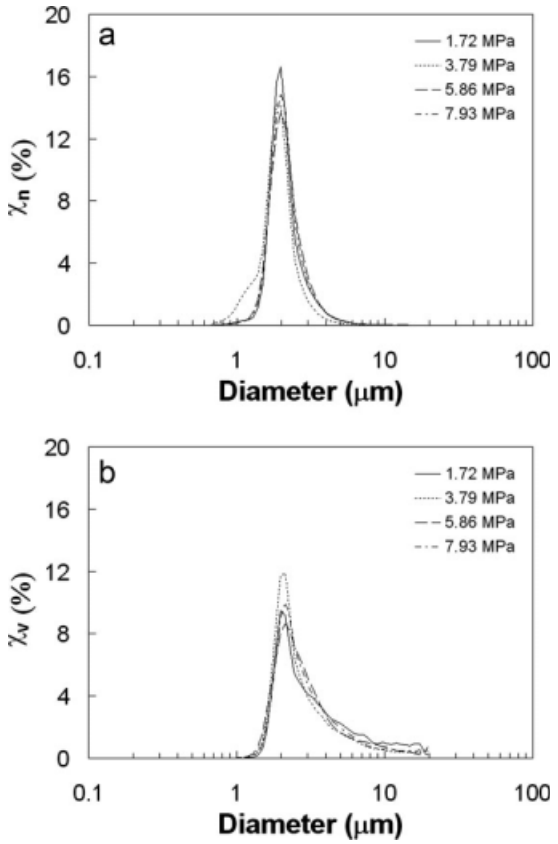

Figure 7. a: Number-weighted distributions of alumina nanopowders expanded from various pressures through a 254 μm × 10 cm nozzle; obtained by averaging the data obtained over several APS measurements. b: Volume-weighted distributions of alumina nanopowders expanded from various pressures through a 254 μm × 10 cm nozzle; obtained by averaging the data obtained over several APS measurements.

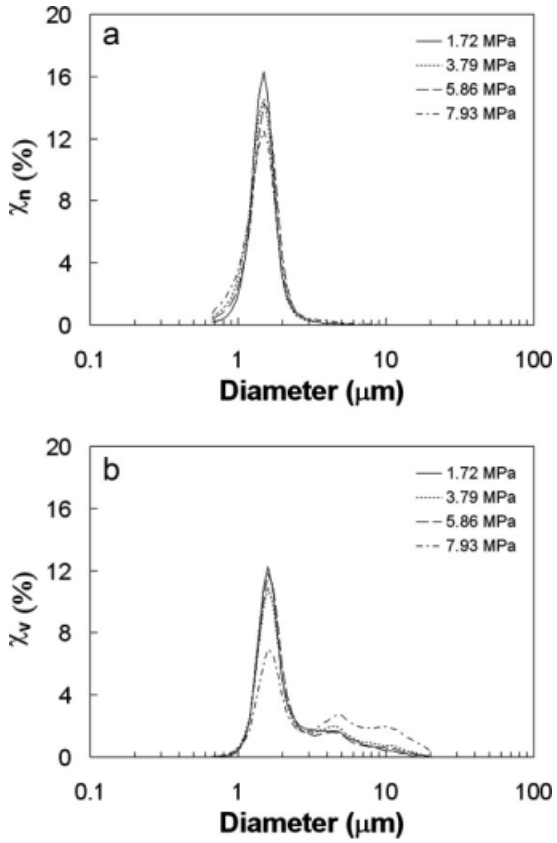

Figure 8. a: Number-weighted distributions of titania nanopowders expanded from various pressures through a 254 μm × 10 cm nozzle; measured by the APS and summed over multiple runs. b: Number-weighted distributions of titania nanopowders expanded from various pressures through a 254 μm × 10 cm nozzle; measured by the APS and summed over multiple runs.

of alumina and titania nanopowders collected on the chip are shown in Figures 9a, b. The number-weighted mode diameters for alumina were all below 400 nm. Similar to the SMPS data (c.f., Table 1), there was no clear trend indicating the effect of pressure on the final agglomerate size. For titania powders, the average agglomerate sizes were below 100 nm, and the size decreased with increasing pressure just like in the SMPS data. The volume-weighted mode diameters appeared to be more erratic, and, given the significant variability in the data and large standard deviations, it was difficult to find a clear trend for both alumina and titania powders. The abundance of submicron agglomerates identified by SEM image analysis agreed with the mixing length-scale observed in alumina and silica mixtures (discussed later in the section for mixing experiments). It should be noted, though, that SEM imaging analysis could also be biased by reagglomeration on the silicon chip surface and the fact that larger agglomerates, due to their inertia, would not diffuse to the chip surface and also could not stay there as easily as the smaller agglomerates.

Experiments on Alumina–Silica Mixing

Returning to the measurements of particle size distributions (following RESS) discussed earlier in this article, SMPS and APS clearly yielded different mode diameters. Although the respective sizing ranges of the SMPS and APS are different and they are expected to produce different results, it is unclear as to which measurement is closer to the actual size of the fragments after RESS/REHPS deagglomeration. It is also striking that under many of the operating conditions both SMPS and APS yielded unimodal size distributions that were within their respective sizing ranges. One can envision two plausible explanations:

(a) The size distribution of the fragments resulting from RESS/REHPS deagglomeration was indeed bimodal due to the competing deagglomeration mechanisms that will be further described in the modeling section.

(b) The primary fragments formed by RESS were in the sub-micron range, close to those measured by SMPS. However, they rapidly reagglomerated in the expansion chamber and the lines leading to the detectors, resulting in peaks detected by the APS that were not necessarily indicative of the primary fragments right after RESS/REHPS deagglomeration. The rather narrow size distributions detected by APS (indicated by similar values for both volume and number weighted modes), along with the fact that the vessel pressure did not have a significant influence over measured agglomerate sizes further suggests this possibility.

In principle, one could move the detectors closer to the tip of the orifice and look for potential shifts in the measured particle size distributions; in practice, however, we had difficulties because both SMPS and APS require constant inflow velocities. Therefore, we decided to use mixing as an indirect method of assessing the typical dimension of the primary fragments.

As mentioned earlier, one of the potential applications of RESS/REHPS deagglomeration of nanopowders would be to

Table 3. Number- and Volume-Weighted Mode Projected Area Diameters and Standard Deviations for Alumina and Titania Nanopowders Expanded Through a 254 μm ID × 10 cm long nozzle

	Alumina				Titania			
	Number Weighted (nm)		Volume Weighted (nm)		Number Weighted (nm)		Volume Weighted (nm)	
Pressure (MPa)	Mode	SD	Mode	SD	Mode	SD	Mode	SD
1.72	61	197	945	299	96	213	1576	715
3.79	243	266	710	273	77	114	609	236
5.86	108	167	774	392	83	119	864	298
7.93	193	177	718	319	49	74	411	144

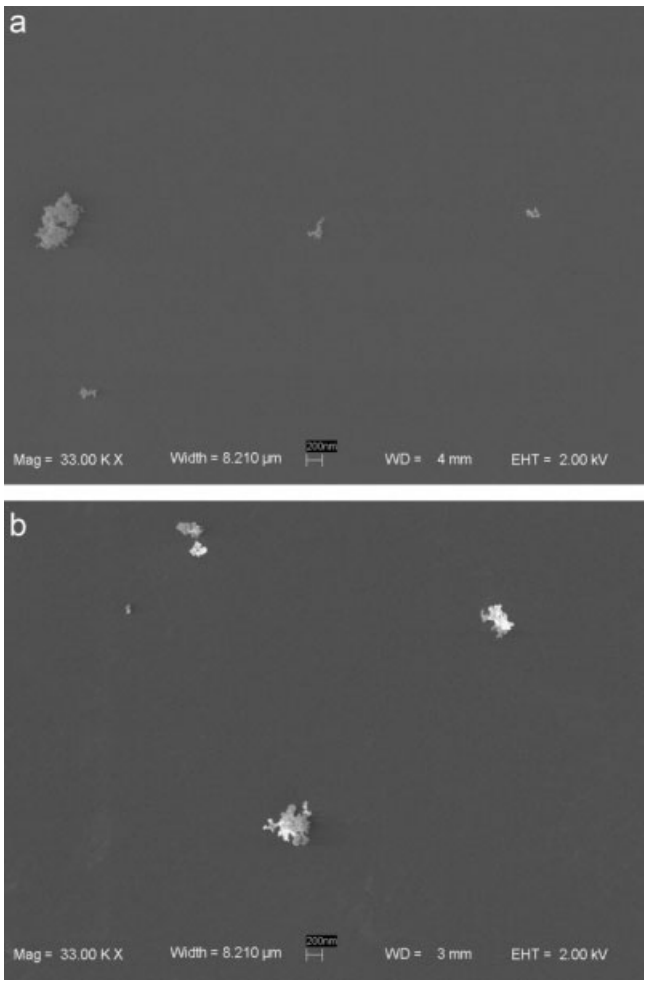

Figure 9. a: Typical micrograph of alumina nanopowders expanded through a 254 μm × 10 cm nozzle. b: Typical micrograph of titania nanopowders expanded through a 254 μm × 10 cm nozzle.

produce intimately mixed nanocomposite materials. When agglomerates of material A and agglomerates of material B (both several microns in size) are suspended in a supercritical (or high-pressure) gas and expanded through a nozzle, these agglomerates will be fragmented simultaneously and mixed at the primary fragment length scale. During reagglomeration, larger agglomerates containing fragments of both A and B may form, but the mixing length-scale between A and B should remain intact. Therefore, by examining the compositions of the agglomerates formed after binary RESS/REHPS mixing experiments, one can retrieve information on the sizes of the primary fragments immediately after RESS/REHPS deagglomeration.

Therefore, binary RESS/REHPS mixing experiments were performed as follows. Mixtures of alumina and silica nanopowders at mullite stoichiometry ($3Al_2O_3{\cdot}2SiO_2$) were suspended in CO_2 and subjected to the RESS/REHPS process. The agglomerates were collected in the expansion chamber and pressed to form a thin tablet. EDS analysis was used in two modes to determine the elemental concentrations (with a resolution of approximately 1 μm) to assess the extent of homogeneity of the mixtures. These modes include: (a) a mapping mode, where a 75 × 50 μm area is scanned and (b) a point analysis, which was used in a quantitative manner, by comparing the statistics developed by determining the elemental concentrations at 100 points (1 μm^2 in size) covering the same 75 × 50 μm area scanned in mode (a). A similar point analysis was performed at three other locations across the tablet, totaling to 400 points. The mixtures were characterized using the intensity of segregation developed by Danckwerts.[52] The intensity of segregation (IOS), described in Eq. 5, is the ratio between the variance, σ,^{2} and the product of the mean concentration of alumina and silica powders, $\mu_{Al_2O_3}$ and μ_{SiO_2}. It ranges between 0, which represents a perfect homogeneity (within the scale of scrutiny, which is 1 μm), and 1, which represents a complete segregation.

$$\mathrm{IOS} = \frac{\sigma^2}{\mu_{Al_2O_3}\mu_{SiO_2}} \tag{5}$$

For comparison, additional EDS scans were performed on a powder mixture produced by shaking the powders in a 65 ml glass jar (but not subjected to RESS/REHPS).

Illustrative EDS scans of the pressed powder mixture produced by shaking are shown in Figures 10a, b; the magnification used in these figures was 5000×. Figure 10a shows the elemental map for aluminum that was used as a measure of the presence of alumina. The light and dark areas represent aluminum-rich and aluminum-deficient regions, respectively. It can be observed that most of this sample was aluminum-rich, except for the upper right and the center which were aluminum-deficient. Figure 10b, a complementary image representing the presence of silicon, shows a similar result with silicon-rich regions occurring in the regions that were deficient in aluminum. These distinct regions of individual constituents as large as 30 μm demonstrate the ineffectiveness of simple shaking in inducing homogeneity at the micron scale. The IOS value for Figures 10a, b is 0.165.

The EDS scans of the powders mixed using the RESS/REHPS process, shown in Figures 11a, b, revealed a constant brightness level across the scan and no distinct regions of either powder, which indicate homogeneity down to a micron. The IOS value for Figures 11a, b is 0.003, almost 2 orders of magnitude smaller than the poorly mixed sample produced by shaking. Although this technique cannot provide information below 1 μm due to the physical limitation of the EDS, it indicates that the mixing length-scale, which is on par with the size of the primary fragments, is below 1 μm. It is very likely that the homogeneity persists at even finer scales: in a comparable study by Yang et al.,[14] by using Electron Energy Loss Spectroscopy, it was shown that RESS/REHPS can indeed achieve sub-micron mixing (c.f., Figure 16b in Yang et al.[14]).

These mixing studies suggest that (a) the size of the primary fragments produced by RESS were closer to those measured by SMPS and SEM analysis, and estimated by the theoretical analysis shown later, and (b) a modest level of reagglomeration likely occurred by the time the expanded suspension reached the APS detector.

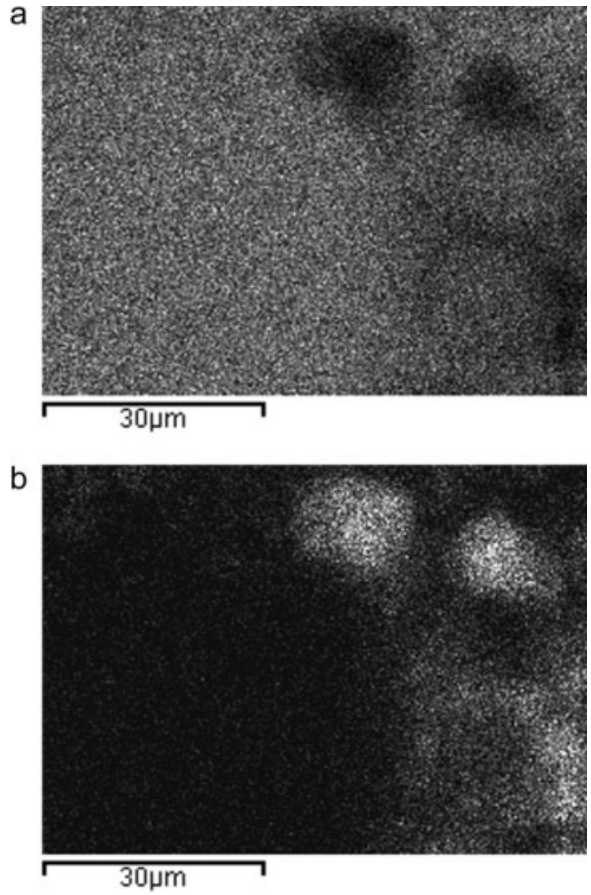

Figure 10. a: Aluminum elemental map of a typical mixture of alumina and silica (stoichiometric ratio of $3Al_2O_3{\cdot}2SiO_2$) produced by hand mixing. b: Silicon elemental map of a typical mixture of alumina and silica (stoichiometric ratio of $3Al_2O_3{\cdot}2SiO_2$) produced by hand mixing.

The deagglomeration and mixing studies presented here clearly demonstrate the efficacy of RESS in producing fragmentation and mixing at the scale of one micron or less.

Models for RESS/REHPS Deagglomeration

It is clear from the experimental data presented earlier that rapid expansion of the gas through a fine nozzle led to breakup of the agglomerates of nanoparticles. The mechanisms through which these size reductions occur are now analyzed. In this section, we apply a one-dimensional compressible flow model to predict the change in CO_2 properties in the nozzle, and use empirical formulas to estimate the strength and position of the Mach disc—an abrupt supersonic-subsonic flow transition that is often featured in the free expansion. Our analysis, described below, suggests that the shear flow in the nozzle and the subsequent impact of the agglomerates with the Mach disc in the free expansion region can both lead to micron or sub-micron level deagglomeration. Complementary two-dimensional numerical simulations, conducted to validate the one-dimensional solutions and to better understand the role of the Mach disc in the deagglomeration process are briefly outlined in the Appendix A.

The RESS/REHPS process has been modeled by many researchers in the literature; for example, refer to Debenedetti,[40] Reverchon and Pallado,[43] Franklin et al.,[53] Hirunsit et al.,[54] Khalil and Miller,[55] and Weber and Thies.[45,46] Therefore, only a skeletal description of the model is presented here and the analysis is limited to conditions close to those employed in our experiments.

Figure 12 shows the system considered in this study, which consists of a mixing chamber (the mixing vessel in Figure 2) filled with CO_2 maintained at specified temperature and pressure, a collection chamber (the expansion tube in Figure 2) that is open to the atmosphere, and a converging section and a straight nozzle connecting the two chambers to expand CO_2 to atmospheric conditions. To facilitate our discussion, six reference points (0–5) are used to separate this system into sections. As the CO_2 leaves the mixing chamber (point 0), it begins to expand first due to the change in the cross-sectional area (from 0 to 1), and then expand under the combined influence of heat transfer and friction (from 1 to 2). Here, ''expand'' only means that the density of CO_2 is

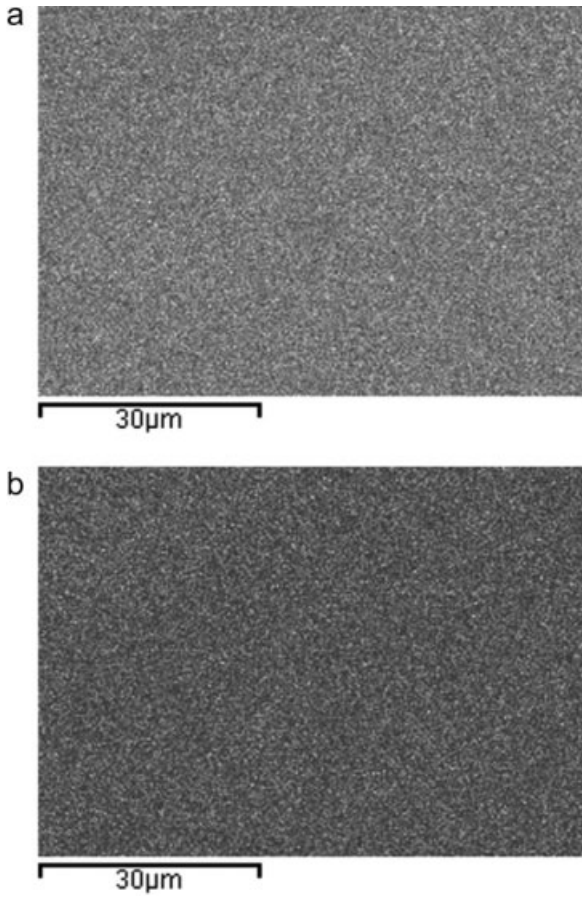

Figure 11. a: Aluminum elemental map of a typical mixture of alumina and silica (stoichiometric ratio of $3Al_2O_3{\cdot}2SiO_2$) produced by RESS mixing. b: Silicon elemental map of a typical mixture of alumina and silica (stoichiometric ratio of $3Al_2O_3{\cdot}2SiO_2$) produced by RESS mixing.

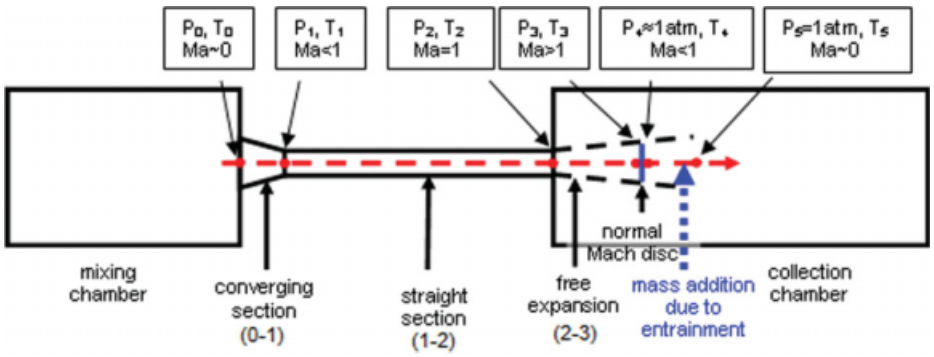

Figure 12. Schematic of the RESS device considered in the modeling study.

[Color figure can be viewed in the online issue, which is available at www.interscience.wiley.com.]

decreasing. Because of the extreme pressure difference between the mixing and collection chambers, the flow in the straight nozzle is choked, i.e., the flow velocity is limited by the speed of sound at the end of the straight nozzle (point 2). Once CO_2 exits the straight nozzle, it undergoes a free expansion, where the temperature and pressure decrease very rapidly in the direction of flow while the velocity turns supersonic. When the pressure drops below collection chamber pressure, a Mach disc is formed (between points 3 and 4). Across this Mach disc, the thermodynamic properties experience step changes: the pressure will increase abruptly to a value slightly lower than the collection chamber pressure, and the gas velocity will drop abruptly from supersonic to subsonic. After that, the expanding gas mixes with the ambient fluid, and reaches the collection chamber pressure at point 5.

Expansion in the converging and straight sections (point 0 to point 2)

To model the flow in the converging and the straight sections (point 0 to point 2), we used a one-dimensional model identical to that in Weber and Thies,[45,46] which contains the following mass, momentum, and energy conservation equations.

$$\begin{aligned} \frac{d\rho}{\rho}+\frac{1}{2}\frac{da^2}{a^2} &= -\frac{1}{A}\frac{dA}{dx}dx \\ \frac{dP}{\rho a^2}+\frac{1}{2}\frac{da^2}{a^2} &= -\frac{2f}{D}dx \\ dh+\frac{1}{2}da^2 &= \frac{w\pi D}{\dot{m}}dx \end{aligned} \tag{6}$$

Here, x is the distance from point 0 to the point of interest, A is the cross-sectional area of the flow device which depends on x, a is the flow velocity, f is the Fanning friction factor of a round pipe, D is the diameter, w is a source term representing heat transfer into the fluid from the walls with a unit of watt per unit area, ρ is the density, P is the pressure, h is the specific enthalpy, and $\dot{m} = \rho A a$ is the mass flow rate. The Fanning friction factor f is a function of the Reynolds number and surface roughness. In this work, we assumed $f = 0.005$ in most of our calculations because this was the value used in all the other one-dimensional RESS/REHPS calculations. According to Perry's Chemical Engineer's Handbook, $f = 0.005$ when Re is about 10^5 and surface roughness λ/D is 0.0008.[56] A sensitivity analysis using another assumed value $f = 0.008$ is included in Table 8.

These equations must be supplemented with a proper equation of state (EOS) so that h can be determined as a function of P and ρ. The EOS proposed by Span and Wagner[57] for CO_2, available in the form of dynamically linkable libraries, was used in our one-dimensional model. This EOS is limited to temperature above 216 K, the triple point of CO_2. If condensation of CO_2 occurs in the expansion process, the model equations would require some modification; however, for the limited objective of the present modeling study, it is sufficient to restrict our attention to those cases where condensation does not occur.

Table 4 lists the conditions at point 2, the tip of the straight nozzle corresponding to different inlet pressures, obtained by integrating the conservation equations (refer Eq. 6) from point 0, the mixing chamber. The numbers in this Table were generated by using the actual size of the expansion device used in our experiments. The inlet diameter D_0, outlet diameter D_1, and the length of the converging section L_{0-1} are 5 mm, 254 μm, and 5 mm, respectively. The diameter $D_{1/2}$ and the length L_{1-2} of the straight nozzle section are 254 μm and 102 mm, respectively. The temperature of the

Table 4. Conditions at the Tip of the Nozzle Corresponding to Various Inlet Pressures, as Predicted by the 1D Model

	Inlet Pressure P_0		
	1.72 MPa	3.79 MPa	5.86 MPa
Pressure P_2	0.42 MPa	0.91 MPa	1.43 MPa
Temperature T_2	270 K	257 K	244 K
Density ρ_2	8.47 kg/m^3	20.4 kg/m^3	37.0 kg/m^3
Velocity V_2	248 m/s	238 m/s	219 m/s
Mass flow rate $\dot{m}$	0.106 gm/s	0.246 gm/s	0.410 gm/s
Kinematic Viscosity v_2	0.016 cm^2/s	0.0064 cm^2/s	0.0034 cm^2/s

CO_2 at the inlet is 318 K, while its pressure is allowed to assume different values as indicated in the Table. As the friction term in Eq. 6 is of the form f/D, it is only important in the straight section where D is at minimum. Thus, friction was only considered in the straight section and neglected in the converging section. Such a simplification was also made in some earlier RESS/REHPS modeling work, e.g., Reverchon and Pallad.[43] In these calculations, the heat transfer term w was set to zero. Note that results are presented only for inlet pressures at or below 5.86 MPa; when the upstream pressure exceeded 5.86 MPa, the analysis predicted that CO_2 condensation can occur in the nozzle. (As aforementioned, our study was limited to cases where such condensation did not occur). This is entirely consistent with our experiments which found evidence for condensation at the highest inlet pressure employed (7.93 MPa), but not at the lower inlet pressures (which were below 5.86 MPa).

Figure 13 shows the variation of pressure, temperature, and density of CO_2 in the RESS device from the mixing chamber (point 0) to the tip of the straight nozzle (point 2) and the Mach number. The initial drop in pressure, temperature, and density from $x = 0$ to $x = 0.005$ (m) is due to the cross-sectional area change in the converging section, and the Mach number reaches about 0.2 at point 1. The subsequent expansion in the straight nozzle (resulting from friction) is more significant than that in the converging section. As x approaches 0.107 m, the end of the nozzle, the dependence of gas properties on x becomes nearly singular due to the subsonic-supersonic transition. The Mach number variations are independent of the initial pressure.

Figure 14 shows the variation of CO_2 velocity and kinematic viscosity as functions of distance in the RESS/REHPS device from point 0 to point 2. The increase in the upstream

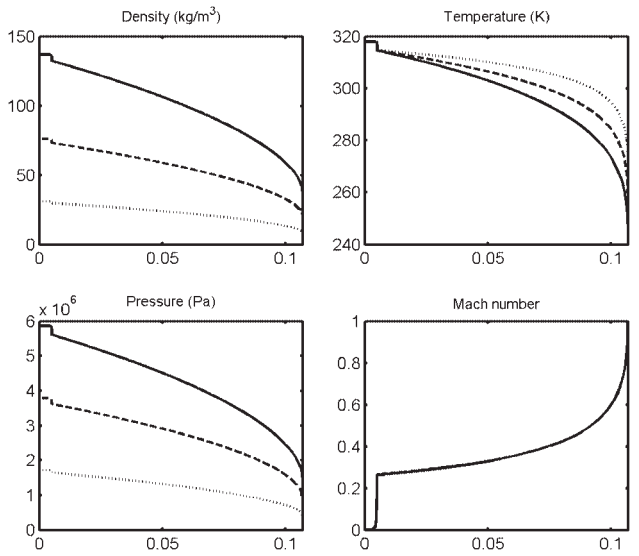

Figure 13. Changes in density, temperature, pressure, and Mach number along the path of expansion (from point 0 to point 2). The horizontal axis is the distance from point 0 measured in meters. Upstream pressure P_0 = 5.86 MPa (solid line), 3.79 MPa (dashed line), and 1.72 MPa (dotted line).

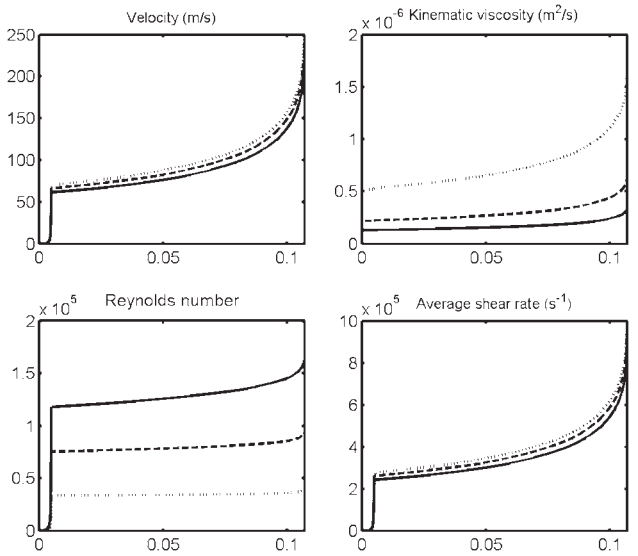

Figure 14. Velocity, kinematic viscosity, average shear rate, and Reynolds number as functions of distance from point 0. Upstream pressure P_0 = 5.86 MPa (solid line), 3.79 MPa (dashed line), and 1.72 MPa (dotted line).

pressure from 1.72 MPa to 5.86 MPa has little effect on the velocities and average shear rates $\dot{\gamma} = V/d$; it, however, reduces the kinematic viscosity, resulting in an increase in the Reynolds number.

It is interesting to note from Table 4 that the velocity V_2 decreases with increasing P_0, contrary to what is expected of incompressible flows. This is because in a choked flow the Mach number at the nozzle tip is always one. As the speed of sound decreases with decreasing temperature and the temperature T_2 drops as one increases P_0, V_2 has to decrease with increasing P_0 to satisfy the choked condition. The mass flow rate increased with increasing pressure in a nonlinear manner. The pressure reduction from point 0 to 2 was approximately a factor of 4 and was nearly independent of P_0.

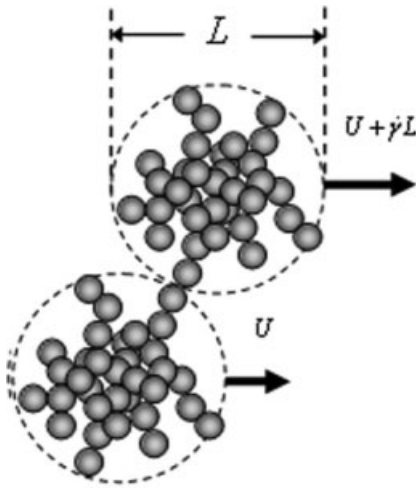

Figure 15. The viscous drag differential acting on two agglomerates of size L in a simple shear flow.

Table 5. Estimates of Location, Size, and Strength of the Mach Disc and the Associated Pressure Changes Across the Mach Disc Assuming $P_4 \approx P_5 = 0.1$ MPa

Inlet Pressure P_0	3.79 MPa	5.86 MPa
Position of the Mach disc (from nozzle tip)	0.69 mm	0.87 mm
Diameter of the Mach disc	0.35 mm	0.44 mm
Mach number before and after the Mach disc	1.94/0.59	2.99/0.48
Pressure before the Mach disc P_3	0.178 MPa	0.192 MPa
Pressure change across the Mach disc	0.077 MPa	0.091 MPa

The conditions at the tip of the nozzle corresponding to these inlet pressures are given in Table 4.

Free expansion from point 2 to point 3

The supersonic free expansion from point 2 to point 3 and the supersonic-subsonic transition from point 3 to point 5, were analyzed as follows:

(a) An empirical relation for position of the Mach disc away from the tip of the nozzle x_M is given by[45,46]:

$$\frac{x_M}{D_2} = 0.67\sqrt{\frac{\tilde{P}_2}{P_4}}, \tag{7}$$

where $\tilde{P}_2$ is the stagnant pressure corresponding to pressure P_2 which, for ideal gas, equals 1.853 P_2 (assuming $C_P/C_V = 1.33$). As the flow after the Mach disc is of low speed, it is safe to assume that $P_4 \approx P_5 = 0.1$ MPa.

(b) An empirical relation for the diameter of the Mach disc D_M is given by:

$$\frac{D_M}{D_2} = 0.42(1 + K_M)\frac{x_M}{D_2}, \tag{8}$$

where $K_M \sim 0.2$[45,46] for CO_2 at the ideal-gas state.

(c) The Mach number immediately before the Mach disc (point 3) is given by[45,46]:

$$\mathrm{Ma}_3 = \left(\frac{D_M}{D_2}\right)^2. \tag{9}$$

(d) The Mach number immediately after the Mach disc (point 4) and the pressure drop across the Mach disc can be obtained using standard normal shock wave tables[58] for ideal gases. (Unlike in the converging section and in the straight nozzle, the supersonic expansion before the Mach disc generally involves very low pressure, temperature, and density of CO_2. Therefore, it is valid to apply equations based on the ideal-gas approximation for CO_2 in this region).

Table 5 presents the values of x_M, D_M, $\mathrm{Ma}_{3/4}$, and the pressure change across the Mach disc corresponding to two different inlet pressures considered earlier in Table 4. At the upstream (inlet) pressure of 1.72 MPa, Eqs. 6–8 do not apply as they predict that $\mathrm{Ma}_3 < 1$, which implies absence of the Mach disc. (Indeed, the 2D simulations discussed in the Appendix A revealed a Mach disc for $P_0 = 2.07$ MPa but not for $P_0 = 1.03$ MPa. Thus, the Mach disc is only present when P_0 is sufficiently high). The data in Table 5 indicate that the distance from the nozzle, diameter, and strength of the Mach disc all increase with increasing inlet pressure.

Shear and impact deagglomeration mechanisms

As hydrodynamic fragmentation of nanoparticle agglomerates is most likely to occur in regions with high velocity gradients and/or rapid property changes, we expect that the deagglomeration observed in the experiments was primarily due to the intense shear in the straight nozzle and the step changes in pressure, density, and temperature associated with the Mach disc.

In a simple model for shear-induced deagglomeration, one can imagine two spherical ''blobs'' of size L, each of which is a fractal ensemble of many primary particles stuck together by the van der Waals force. The blobs will experience a velocity difference of $\dot{\gamma}L$ in a shear flow with shear rate $\dot{\gamma}$ (refer an illustration in Figure 15) that leads to a drag differential between the two blobs

$$F_{\mathrm{shear}} = 3\pi\mu\dot{\gamma}L^2 \tag{10}$$

The cohesive forces between agglomerates were estimated as the van der Waals force between two primary alumina particles of diameter L_P (assuming the particles are spherical), and is given by

$$F_{\mathrm{VdW}} = \frac{L_P}{24}\frac{H}{\Delta^2}. \tag{11}$$

Here, H is the Hamaker constant, which is typically 10^{-19} J between metal oxide spheres submerged in a non-polar solvent,[59] and Δ is a parameter controlling the maximum cohesive strength between primary particles that can be understood as the closest approach between two primary particles. On the macroscopic level, a higher Δ generally leads to a lower surface energy of the material. In the illustrative calculations below, we consider two different values for Δ: 1 nm and 0.5 nm representing different level of cohesion, and use $L_P \sim 13$ nm and 21 nm (alumina and titania primary particles). Letting $F_{\mathrm{shear}} = F_{\mathrm{VdW}}$ and substituting $\dot{\gamma} = V_2/D_2$ into Eq. 10, we obtain L to be ~700 nm for alumina and 800–900 nm for titania when $\Delta = 1$ nm, and 1300–1400 nm (alumina) and 1700–1800 nm (titania) when $\Delta = 0.5$ nm

Table 6. Estimates for the Average Size of Agglomerates After Passing Through the Nozzle, as Determined by Equating the Shear-Induced Viscous Drag Differential (Eq. 6) and the van der Waals force (Eq. 7)

Pressure P_0	$L_P = 13$ nm, $\Delta = 1$ nm	$L_P = 13$ nm, $\Delta = 0.5$ nm	$L_P = 21$ nm, $\Delta = 1$ nm	$L_P = 21$ nm, $\Delta = 0.5$ nm
1.72 MPa	0.66 μm	1.32 μm	0.84 μm	1.68 μm
3.79 MPa	0.69 μm	1.38 μm	0.88 μm	1.76 μm
5.86 MPa	0.73 μm	1.46 μm	0.93 μm	1.85 μm

Table 7. Estimated Average Agglomerate Size L After the Suspension Passes Through the Mach Disc (Eq. 9)

Collection Chamber Pressure P_4	Mixing Chamber Pressure P_0	Mach Number and Pressure Change Across the Mach Disc	Alumina ($\Delta = 0.5$ nm)	Titania ($\Delta = 0.5$ nm)
0.1 MPa	3.79 MPa	Ma = 1.94 ΔP = 0.077 MPa	0.30 μm	0.38 μm
	5.83 MPa	Ma = 2.98 ΔP = 0.091 MPa	0.28 μm	0.35 μm

(Table 6). The order of magnitude of these numbers are in good agreement with the average size of agglomerates observed in our experiments, and suggest that the shear in the straight nozzle does play an important role in the deagglomeration process. Interestingly, due to the drastic reduction in the kinematic viscosity of the fluid at elevated pressures, L increases slightly with increasing inlet pressure P_0.

Impact deagglomeration may also be an important aspect of the RESS/REHPS process. As an agglomerate of nanoparticles passes through the Mach disc, the rapid changes in pressure, density, and velocity across the Mach disc produce an impulse that may shatter the agglomerate into many smaller pieces. The experimental studies by Brandt et al.[34] and by Strecker and Roth[60] showed that normal shock waves were very effective in reducing the average agglomerate size in a shock tube. In Brandt et al.,[34] the reduction in agglomerate size was correlated to the pressure drop across the normal shock, and agglomerates consisting of 40 nm SiO_2 primary particles were fragmented to an average size of 400–500 nm when the pressure drop across the normal shock was about 0.1 MPa. In Strecker and Roth,[60] as the primary particles were of a larger size (325 nm), the agglomerates were primarily in the form of dimers and trimers. After a normal shock wave passed through, the fractions of dimers and trimers were significantly reduced.

We model the effect of the Mach disc on the deagglomeration by setting the force acting on an agglomerate of size L due to the sudden pressure increase across the Mach disc to be proportional to the van der Waals binding force between a pair of primary particles

$$\frac{\Delta P \pi L^2}{4} \propto \frac{L_P H}{24\Delta^2} \tag{12}$$

Rearranging,

$$L = \alpha \sqrt{\frac{L_P H}{6\pi \Delta P \Delta^2}} \tag{13}$$

where α is a proportionality constant. The experimental data of Brandt et al.[34] for agglomerates containing spherical SiO_2 primary particles conform reasonably well with this formula and yield $\alpha \sim 5$ (assuming $\Delta = 0.5$ nm in their experiments). (If one assumes that $\Delta = 1.0$ nm in their experiments, then the estimated value of α would be $\sim$10). The average agglomerate size L after the suspension passes through the Mach disc, estimated by substituting the ΔP across the Mach disc listed in Table 5, $\alpha = 5$ and $\Delta = 0.5$ nm into Eq. 13, are presented in Table 7; it can be seen that the values of L are about 300 nm for alumina agglomerates, and 350–400 nm for titania agglomerates. The order-of-magnitude agreement between these numbers and the average sizes observed in our experiments suggests that impact with the Mach disc may also be an effective deagglomeration mechanism in the RESS/REHPS process. In contrast with Table 6, here L decreases slightly with increasing inlet pressure.

The data in Tables 6 and 7 suggest that the effect of inlet pressure P_0 on deagglomeration is complex. On one hand, an elevated P_0 increases the strength of the Mach disc; on the other hand, it reduces the viscosity of the fluid and the shear stresses in the nozzle. Therefore, when the two mechanisms work together, the agglomerate size may become insensitive to the change in P_0. Indeed, in the experiments, the size of neither alumina nor titania powders changed significantly in the pressure range of 1.72–5.86 MPa.

Using the flow models for RESS/REHPS and the deagglomeration analyses presented earlier, the sensitivity of the final agglomerate sizes resulting from shear and impact, respectively, to various experimental parameters such as the inlet temperature, nozzle diameter, length, Fanning friction factor f, and heat transfer rate w were tested. Table 8 summarizes some illustrative examples.

The Fanning friction factor f is largely an unknown parameter because it is a function of the Reynolds number, which varies with position in the nozzle and depends on the upstream conditions, and the roughness of the inner surface, which is difficult to measure for a thin nozzle. Although we do not know what f is for our particular RESS/REHPS system, it is possible to substitute a different f into the 1D model and study its influence on the model predictions. In Table 8, it can be observed that raising f from 0.005 to 0.008 reduces the pressure and density at nozzle exit and the flow rate. However, due to the increase in the kinematic viscosity, L_{shear} is not significantly changed. The influence on the free expansion and L_{impact} is also very small. This calculation shows that deagglomeration is not very sensitive to the friction factor.

Raising the inlet temperature T_0 from 318 K to 370 K decreases the mass flow rate through the nozzle (in agreement with Reverchon and Pallado[43]), but increases the velocity and kinematic viscosity at the exit. As a result, the shear in the straight nozzle becomes more effective in reducing the size of the agglomerates—the estimated agglomerate size is reduced by 13% from 1.37 μm to 1.19 μm. The change in inlet temperature, however, does not have any significant influence on the free expansion—the changes in the position and Mach number of the Mach disc are marginal and have no effect on deagglomeration.

As rapid expansion of supercritical CO_2 is always accompanied by strong reduction in temperature, heat transfer from the ambient to the nozzle is bound to occur in a RESS/REHPS process. Even though the rate of heat transfer in our experiments is not known quantitatively, its effect can be studied in a qualitative manner by assigning a non-zero value to the heat source term w in Eq. 6. As shown in Table 8, the effect of supplying heat to the nozzle is very similar

Table 8. Effect of Inlet Condition and Nozzle Diameter and Length on the State of CO_2 at the Tip of the Nozzle and Near the Mach Disc

Initial Condition/ Nozzle Dimension	Properties at the Tip of the Nozzle	Properties of the Mach Disc
Reference system		
$P_0 = 3.79$ MPa	$P_2 = 0.91$ MPa, $T_2 = 257$ K	$x_M = 0.69$ mm, $D_M = 0.35$ mm
$T_0 = 318$ K	$\rho_2 = 20.4$ kg/m^3, $V_2 = 238$ m/s	$Ma_3 = 1.94$, $Ma_4 = 0.59$
$L_{0-1} = 5$ mm	$\dot{m} = 0.246$ gm/s, $\nu = 0.0064$ cm^2/s	$\Delta P = 0.077$ MPa,
$f = 0.005$	$L_{shear} = 1.37$ μm	$L_{impact} = 0.30$ μm
No heat transfer		
$D_{1/2} = 254$ μm		
$L_{1-2} = 102$ mm		
Same as the reference system except		
$f = 0.008$	$P_2 = 0.76$ MPa, $T_2 = 254$ K	$x_M = 0.64$ mm, $D_M = 0.32$ mm
	$\rho_2 = 17.0$ kg/m^3, $V_2 = 239$ m/s	$Ma_3 = 1.82$, $Ma_4 = 0.61$
	$\dot{m} = 0.208$ gm/s, $\nu = 0.0075$ cm^2/s	$\Delta P = 0.073$ MPa
	$L_{shear} = 1.38$ μm	$L_{impact} = 0.31$ μm
Same as the reference system except		
$T_0 = 370$ K	$P_2 = 0.94$ MPa, $T_2 = 314$ K	$x_M = 0.70$ mm, $D_M = 0.36$ mm
	$\rho_2 = 16.5$ kg/m^3, $V_2 = 262$ m/s	$Ma_3 = 1.95$, $Ma_4 = 0.59$
	$\dot{m} = 0.220$ gm/s, $\nu = 0.0095$ cm^2/s	$\Delta P = 0.077$ MPa
	$L_{shear} = 1.19$ μm	$L_{impact} = 0.30$ μm
Same as the reference system except heat transfer		
$w = 10^5$ watt/m^2	$P_2 = 0.95$ MPa, $T_2 = 291$ K	$x_M = 0.71$ mm, $D_M = 0.36$ mm
	$\rho_2 = 18.4$ kg/m^3, $V_2 = 252$ m/s	$Ma_3 = 1.98$, $Ma_4 = 0.58$
	$\dot{m} = 0.234$ gm/s, $\nu = 0.0080$ cm^2/s	$\Delta P = 0.078$ MPa
	$L_{shear} = 1.25$ μm	$L_{impact} = 0.30$ μm
Same as the reference system except		
$D_{1/2} = 350$ μm	$P_2 = 1.03$ MPa, $T_2 = 259$ K	$x_M = 1.02$ mm, $D_M = 0.51$ mm
	$\rho_2 = 23.0$ kg/m^3, $V_2 = 236$ m/s	$Ma_3 = 2.14$, $Ma_4 = 0.56$
	$\dot{m} = 0.524$ gm/s, $\nu = 0.0057$ cm^2/s	$\Delta P = 0.082$ MPa
	$L_{shear} = 1.61$ μm	$L_{impact} = 0.29$ μm
Same as the reference system except		
$L_{1-2} = 50$ mm	$P_2 = 1.16$ MPa, $T_2 = 261$ K	$x_M = 0.78$ mm, $D_M = 0.40$ mm
	$\rho_2 = 26.1$ kg/m^3, $V_2 = 236$ m/s	$Ma_3 = 2.43$, $Ma_4 = 0.52$
	$\dot{m} = 0.313$ gm/s, $\nu = 0.0051$ cm^2/s	$\Delta P = 0.086$ MPa
	$L_{shear} = 1.36$ μm	$L_{impact} = 0.28$ μm
Same as the reference system except		
$L_{1-2} = 2.6$ mm	$P_2 = 1.93$ MPa, $T_2 = 273$ K	$x_M = 1.01$ mm (0.72 mm), $D_M = 0.51$ mm (0.36 mm)
	$\rho_2 = 43.8$ kg/m^3, $V_2 = 236$ m/s	
	$\dot{m} = 0.523$ gm/s, $\nu = 0.0032$ cm^2/s	$Ma_3 = 4.02$ (2.04), $Ma_4 = 0.43$ (0.57)
	$L_{shear} = 1.33$ μm	
		$\Delta P = 0.095$ MPa (0.157 MPa)
		$L_{impact} = 0.27$ μm (0.21 μm)

L_{shear} and L_{impact} represent the estimated agglomerate size after deagglomeration assuming $L_P = 13$ nm, $H = 10^{-19}$ J, and $\Delta = 0.5$ nm. For the last row, the numbers in the parentheses represent the expected changes if P_4 is raised from 0.1 MPa to 0.2 MPa.

to that of raising the inlet temperature. It increases the temperature, velocity, and kinematic viscosity of CO_2 at the tip of the nozzle, and has a positive influence on deagglomeration. Note that $w = 10^5$ watt/m^2 is a very high rate of heat transfer; yet, our calculation indicates only small effects on L_{shear} and L_{impact}. Thus, in practical RESS systems the heating of the nozzle, while important in keeping dry ice from forming, does not play a major role in deagglomeration.

Table 8 then lists the conditions one would expect at the tip of the nozzle and near the Mach disc when the nozzle diameter is increased from 254 μm to 350 μm. Increasing nozzle diameter reduces the shear and the flow resistance and raises the flow rate of CO_2 significantly. This decreases the efficiency of deagglomeration in the nozzle, but increases the Mach number and pressure change across of the Mach disc.

Finally, it is shown in Table 8 that a shorter nozzle leads to a higher shear rate in the nozzle and a higher Mach number in the free expansion, thus helping to reduce the agglomerate size. It is interesting to note that even though the Mach number reaches a very high value of 4.02 and P_3 drops down to 1/18 of P_4 for the shortest nozzle (2.6 mm in length), the pressure change across the Mach disc $P_4 - P_3$ is only 0.095 MPa. This observation suggests that to exploit the pressure change across the Mach disc to fragment the agglomerates, one could increase P_4 and P_5 to achieve higher ΔP and better deagglomeration. For example, if CO_2 is expanded into a pressurized chamber with $P_4 = 0.2$ MPa using the short nozzle (0.26 cm), while Ma_3 is reduced from 4.02 to 2.03, the pressure drop across the Mach disc is increased from 0.095 MPa to 0.157 MPa and Eq. 13 predicts a decrease in the agglomerate size from 270 nm to 210 nm.

The above sensitivity analysis reveals that while there is room for optimizing the RESS process design, the typical agglomerate sizes undergo only incremental changes with changes in the process conditions; in other words, the agglomerate size estimates obtained in the above analysis are robust.

In this section, we treated the free expansion zone empirically and some concerns remain about the reliability of the Mach disc properties and deagglomeration at this location. In

general, not all the gas issuing out of the orifice will pass through the Mach disc, and only a fraction of the agglomerates coming out of the nozzle will experience the impact force. Many experiments and two-dimensional simulations indicate that in a RESS process only about 50% of the mass would pass through the Mach disc.[44,45,51,54,61] To check the flow behavior in the free expansion zone, steady 2D (axisymmetric) computational fluid dynamics (CFD) simulations were performed using a commercial software Fluent®. The results of these CFD simulations are presented in the Appendix A. Our simulations suggest that only about 50% of the mass would pass through the Mach disc for $P_0 = 5.86$ MPa, while for the lower pressures the fraction of agglomerates passing through the Mach disc is even less. Furthermore, Mach disc was only present when P_0 is sufficiently high, consistent with the predictions of the empirical formulas; deagglomeration occurred even in the cases where the Mach disc was absent. These considerations suggest that shattering at the Mach disc alone is not likely to be the dominant mechanism and that shear in the nozzle must be contributing appreciably to the deagglomeration observed in the experiments.

Summary

Deagglomeration of suspensions of nanoparticle aggregates via rapid expansion of supercritical or high-pressure suspensions has been investigated experimentally, as well as complementary modeling study and mixing experiments. The size distribution of fragmented nanopowders exiting the nozzle attached to a pressure vessel was characterized via online SMPS and APS and off-line SEM imaging.

The number- and volume-weighted mode diameters of expanded alumina and titania measured by the SMPS, listed in Table 1, show that the nanopowders are significantly deagglomerated by the RESS/REHPS process. The number-weighted mode diameters were all below 100 nm, and the effect of pressure was rather weak; at the highest pressure, the number-weighted mode diameters of alumina and titania fragments were 35 nm and 37 nm, respectively. The volume-weighted size distributions indicate that although agglomerates larger than the SMPS measurement size limit of 572.5 nm were indeed likely to be present, the volume-weighted mode was below 400 nm for both nanopowders for pressures above 1.72 MPa. At the higher pressures, from 3.79 to 7.93 MPa, there was a trend of decreasing fragment size with increasing pressure. Thus, the SMPS results clearly indicated that most of the fragments resulting from the RESS process (on a volume basis) were below half micron in size, while the majority of them were under 100 nm in size; as some reagglomeration could have occurred during the SMPS sampling, the actual sizes could have been even smaller than these values. Selected REHPS experiments performed using nitrogen instead of CO_2 indicate that the results are comparable and hence alternate gases may be used for the purpose of deagglomeration.

The APS measurements showed that most of the agglomerates had aerodynamic diameters between 1 and 3 μm; furthermore, since the number- and volume-weighted modes were similar, the agglomerate size distribution was not wide. It was also shown that while there is an uncertainty regarding the value of the agglomerate density, the APS results are not too sensitive to its assumed value.

The deagglomeration results from SEM analysis indicated that number-weighted mode diameters for alumina were all below 400 nm, while those for titania were below 100 nm. The volume-weighted mode diameter appeared to decrease with increasing mixing chamber pressure. For alumina, the volume-weighted mode at the higher pressures were all between 700 and 800 nm, while, for titania, they showed a more drastic change with increasing pressure, as the value went down to about 400 nm at the highest pressure. While there was a significant amount of variability in this data, the results were closer to the SMPS results than to the APS results, and were also comparable to the scale of mixing achieved for the RESS/REHPS-processed mixtures of alumina and silica nanopowders at mullite stoichiometry. The EDS scans of the mixed powders revealed a constant brightness level across the scan and no distinct alumina or silica rich regions, and thus indicating excellent mixture uniformity at a scale of one micron or smaller.

On the basis of the overall deagglomeration results and the sample mixing study, it can be concluded that RESS/REHPS led to fragments which were at the sub-micron scale, and more likely to be less than 0.5 micron in size. The higher values reported by the APS are indicative of reagglomeration during sampling.

Overall, the results from the deagglomeration in the RESS/REHPS process considered here are comparable to or better than those in Brandt et al.,[34] where the reduction in agglomerate size was correlated to the pressure drop across the normal shock. It is noted that in their studies, the agglomerates consisting of 40 nm SiO_2 primary particles (in contrast to our particles of about 20 nm) were fragmented to a number (or count) average size of 400–500 nm when the pressure drop across the normal shock was about 0.1 MPa. Our number-average was significantly below that range and typically smaller than 100 nm.

The mechanisms through which a reduction in the size of the agglomerates occurs via the RESS/REHPS process were also analyzed using a one-dimensional compressible flow model to predict the change in CO_2 properties in the nozzle, along with the use of empirical formulas to estimate the strength and position of the Mach disc in the free expansion region. The one-dimensional model used in our analysis is identical to that used by Weber and Thies,[45,46] and is utilized for the purpose of understanding the mechanisms of agglomerate break-up. Our analysis examined both the shear-induced break-up in the nozzle and the impact break-up at the Mach disc. Although all of the agglomerates in the flow experience the break-up due to shear, it is estimated through 2D simulations of flow in the free jet that only about half would pass through the Mach disc. The results suggest that the shear flow in the nozzle and the subsequent impact of the agglomerates with the Mach disc in the free expansion can both lead to micron or sub-micron level deagglomeration. These results are supported by our experimental observations. Furthermore, sensitivity analysis based on this model revealed that the characteristic fragment size was robust, changing only modestly with operating conditions such as the mixing chamber pressure; thus, deagglomeration by RESS can indeed be achieved over a broad range of operating conditions.

As dry nanoparticles are invariably present as large fractal agglomerates that are tens or hundreds of microns in size, dry

mixing of the individual nanoparticle constituents at the submicron scale is not easily achieved unless an effective deagglomeration step is included in the process. The RESS/REHPS process discussed in this article achieves such fragmentation and is therefore of value in mixing nanoparticle agglomerates, which can subsequently be processed to make nanocomposites of superior properties than feasible otherwise.

Acknowledgments

This study was supported by the National Science Foundation through a NIRT grant, DMI-0506722, and an IGERT fellowship to D.T. via DGE-0504497. Partial support from EEC-0540855 to R.N.D. is also acknowledged. The authors acknowledge the assistance in conducting some of the mixing experiments from Mark Panczyk, an NSF-REU student at NJIT, supported through EEC-0540855.

Literature Cited

1. Imanaka N, Kohler J, Masui T, Adachi GY, Taguchi E, Mori H. Inclusion of nanometer-sized Al_2O_3 particles in a crystalline (Sc, Lu)2(WO4)3 matrix. *J Am Ceram Soc*. 2000;83:427–429.
2. Lines MG. Nanomaterials for practical functional uses. *J Alloys Comp*. 2008;449:242–245.
3. Roco MC. Nanoparticles and nanotechnology research. *J Nanoparticle Res*. 1999;1:1–6.
4. Friedlander SK. *Smoke, Dust, and Haze: Fundamentals of Aerosol Dynamics*. New York, NY: Oxford University Press, 2000.
5. Nam CH, Pfeffer R, Dave RN, Sundaresan S. Aerated vibrofluidization of silica nanoparticles. *AIChE J*. 2004;50:1776–1785.
6. Yu Q, Dave RN, Zhu C, Quevedo JA, Pfeffer R. Enhanced fluidization of nanoparticles in an oscillating magnetic field. *AIChE J*. 2005;51:1971–1979.
7. Kurkela JA, Brown DP, Raula J, Kauppinen EI. New apparatus for studying powder deagglomeration. *Powder Technol*. 2008;180:164–171.
8. Yao W, Suangsheng G, Fei W, Jun W. Fluidization and agglomerate structure of SiO2 nanoparticles. *Powder Technol*. 2002;124:152–159.
9. Van der Wel PGJ. Powder mixing. *Powder Handling Processing*. 1999;11:83–86.
10. Fan LT, Chen YM, Lai FS. Recent developments in solids mixing. *Powder Technol*. 1990;61:255–287.
11. Iwasaki T, Satoh M. Characterization of powder mixers based on mechanical energy using soft dye granules. *Adv Powder Technol*. 2002;13:395–409.
12. Vaizoglu O. Assessment of the degree of mix of powder mixtures. *Turk J Phys*. 1999;23:97–104.
13. Wei D, Dave RN, Pfeffer R. Mixing and characterization of nanosized powders: an assessment of different techniques. *J Nanoparticle Res*. 2002;4:21–41.
14. Yang J, Wang Y, Dave RN, Pfeffer R. Mixing of nanoparticles by rapid expansion of high pressure suspensions. *Adv Powder Technol*. 2003;14:471–493.
15. Scicolone J, Sanganwar G, To D, Ermoline A, Dave RN, Gupta RB, Pfeffer R. Deagglomeration and Mixing of Nanoparticles. Proceedings of Partec 2007 Meeting. Nuremburg, Germany, 2007:8–10.
16. Barrow R, Yang J, Dave RN, Pfeffer R. Dry-Mixing of Sub-Micron Size B and BaCrO4 Particles for Use in T-10 Delay Composition. Proceedings (CD-ROM) of Fifth World Congress on Particle Technology. Orlando, FL, 2006: disk-II, paper 70c:1–6.
17. Marioth E, Kroeber H, Loebbecke S, Fuhr I, Krause H. Deagglomeration and Mixing of Nanoparticles Using the Rapid Expansion of Supercritical Dispersions. Proceedings of Partec Meeting 2007. Nuremburg, Germany, 2007:S31–1.
18. Nelson K, Deng Y. Effect of polycrystalline structure of TiO2 particles on the light scattering efficiency. *J Colloid Interface Sci*. 2008;319:130–139.
19. Seekkuarchchi N, Kumazawa H. Aggreagation and disruption mechanisms of nanoparticulate aggregates. 2. Dispersion of aggregates using a motionless mixer. *Ind Eng Chem Res*. 2008;47:2401–2413.
20. Ding P, Pacek AW. Effect of pH on deagglomeration and rheology/morphology of aqueous suspension of goethite nanopowder. *J Colloid Interface Sci*. 2008;325:165–172.
21. Shinohara N, Dabbs DM, Aksay IA. Infrared transparent mullite through densificiation of monolithic gels at 1250 degrees celcius. *Infrared Opt Trans Mater*. 1986;683:19–24.
22. Oliveira MILL, Chen K, Ferreira JMF. Influence of the deagglomeration procedure on aqueous dispersion, slip casting and sintering of Si3N4-based ceramics. *J Eur Ceram Soc*. 2002;22:1601–1607.
23. Hellmig RJ, Ferkel H. Effect of nanopowder deagglomeration on the densities of nanocrystalline ceramic green bodies and their sintering behavior. *NanoStructured Mater*. 1999;11:617–622.
24. Aoki M, Ring TA, Haggerty JS. Analysis and modeling of the ultrasonic dispersion technique. *Adv Ceram Mater*. 1987;2:209–212.
25. Ding P, Pacek AW. De-agglomeration of goethite nanoparticles using ultrasonic comminution device. *Powder Technol*. 2008;187:1–10.
26. Uhland SA, Cima MJ, Sachs EM. Additive-enhanced redispersion of ceramic agglomerates. *J Am Ceram Soc*. 2003;86:1487–1492.
27. Le Bars N, Levitz P, Messier A, Francois M, Van Damme H. Deagglomeration and dispersion of Barium Titanate and alumina particles in an organic medium. *J Colloid Interface Sci*. 1995;175:400–410.
28. Sanganwar GP, Gupta RB, Ermoline A, Scicolone JV, Dave RN. Environmentally benign nanomixing by sonication in high pressure carbon dioxide. *J Nanoparticle Res*. 2009;11:405–419.
29. Nakamura H, Watano S. Fundamental particle fluidization behavior and handling of nanoparticles in a rotating fluidized bed. *Powder Technol*. 2008;183:324–332.
30. Endo Y, Hasebe S, Kousaka Y. Dispersion of aggregates of the powder by acceleration in an air stream and its application to the evaluation of adhesion between particles. *Powder Technol*. 1997;91:25–30.
31. Voss A, Finlay WH. Deagglomeration of dry powder pharmaceutical aerosols. *Int J Pharma*. 2002;248:39–50.
32. Weimar AW, Cochran GA, Henley JP, Hook BD, Mills LK. Rapid process for manufacturing aluminum nitride powder. *J Am Ceram Soc*. 1994;77:3–18.
33. Koybayashi Y. Studies of aggregation effects on sox removal by limestone powder. *AIChE J*. 1995;41:2642–2652.
34. Brandt O, Rajahusmi AM, Roth P. First observations on break up of particle agglomerates in shock waves. *Exp Fluids*. 1987;5:86–94.
35. Jung J, Perrut M. Particle design using supercritical fluids: literature and patent survey. *J Supercrit Fluids*. 2001;20:179–219.
36. Reverchon E. Supercritical antisolvent precipitation of micro and nanoparticles. *J Supercrit Fluids*. 1999;15:1–21.
37. Yeo SD, Kiran E. Formation of polymer particles with supercritical fluids: a review. *J Supercrit Fluids*. 2005;34:287–308.
38. Shariati A, Peters CJ. Recent developments in particle design using supercritical fluids. *Curr Opin Solid State Mater Sci*. 2003;7:371–383.
39. Hakuta Y, Hayashi H, Arai K. Fine particle formation using supercritical fluids. *Curr Opin Solid State Mater Sci*. 2003;7:341–351.
40. Debenedetti PG. Homogeneous nucleation in supercritical fluids. *AIChE J*. 1990;36:1289–1298.
41. Debenedetti PG, Tom JW, Kwauk X, Yeo SD. Rapid expansion of supercritical solutions (RESS): fundamentals and applications. *Fluid Phase Equilibria*. 1993;82:311–321.
42. Kwauk X, Debenedetti PG. Mathematical modeling of aerosol formation by expansion of supercritical solutions in converging nozzles. *J Aerosol Sci*. 1994;24:445–469.
43. Reverchon E, Pallado P. Hydrodynamic modeling of the RESS process. *J Supercrit Fluids*. 1996;9:216–221.
44. Weber M, Russell LM, Debenedetti PG. Mathematical modeling of nucleation and growth of particles formed by the rapid expansion of a supercritical solution under subsonic conditions. *J Supercrit Fluids*. 2002;23:65–80.
45. Weber M, Thies MC. Understanding the RESS process. In: Sun YP, editor. *Supercritical Fluid Technology in Materials Science and Engineering: Syntheses, Properties, and Applications*. 2002.
46. Weber M, Thies MC. A simplified and generalized model for the rapid expansion of supercritical solutions. *J Supercrit Fluids*. 2007;40:402–419.
47. Wang HW, John W. Particle density correction for the aerodynamic particle sizer. *Aerosol Sci Technol*. 1987;6:191–198.

48. Valverde JM, Quintanilla MAS, Castellanos A, Lepek D, Quevedo J, Dave RN, Pfeffer R. Fluidization of fine and ultrafine particles using nitrogen and neon as fluidizing gases. *AICHE J*. 2008;54:86–103.
49. Sun M, Hsu TJ. Flocculation model of cohesive sediment using variable fractal dimension. *Environ Fluid Mech*. 2008;8:55–71.
50. Khelifa A, Hill PS. Models for effective density and settling velocity of flocs. *J Hydraul Res*. 2006;44:390–401.
51. Maggi F, Mietta F, Winterwerp JC. Effect of variable fractal dimension on the floc size distribution of suspended cohesive sediment. *J Hydrol*. 2007;343:43–55.
52. Danckwers PV. The definition and measurement of some characteristics of mixtures. *Appl Sci Res*. 1952;3:279–296.
53. Franklin RK, Edwards JR, Chernyak Y, Gould RD, Henon F, Carbonell RG. Formation of perfluoropolyether coatings by the rapid expansion of supercritical solutions (RESS) process. Part 2: Numerical modeling. *Ind Eng Chem Res*. 2001;40:6127–6139.
54. Hirunsit P, Huang Z, Srinophakun T, Charoenchaitrakool M, Kawi S. Particle formation of ibuprofen-supercritical CO_2 system from rapid expansion of supercritical solutions (RESS): a mathematical model. *Powder Technol*. 2005;154:83–94.
55. Khalil I, Miller DR. The structure of supercritical fluid free-jet expansions. *AICHE J*. 2004;50:2697–2704.
56. Green DG, Perry RH. *Perry's Chemical Engineers' Handbook*, 8th ed. New York, NY: McGraw-Hill, 2007.
57. Span R, Wagner W. A new equation of state for carbon dioxide covering the fluid region from the triple-point temperature to 1100 K at pressures up to 800 MPa. *J Phys Chem Ref Data*. 1996;25:1509–1596.
58. Hodge BK, Koenig K. *Compressible Fluid Dynamics: With Personal Computer Applications*. Englewood Cliffs: Prentice Hall, 1995.
59. Lide DR. *CRC Handbook of Chemistry and Physics*, 88th ed. Cleveland, OH: CRC Press, 2007.
60. Strecker JJF, Roth P. Particle breakup in shock waves studied by single particle light scattering. *Part Part Syst Charact*. 1994;11:222–226.
61. Chernyak Y, Henon F, Harris RD, Gould RD, Franklin RK, Edwards JR, DeSimone JM, Carbonell RG. Formation of perfluoropolyether coatings by the rapid expansion of supercritical solutions (RESS) process. Part 1: Experimental results. *Ind Eng Chem Res*. 2001;40:6118–6126.
62. Lele AK, Shine AD. Morphology of polymers precipitated from a supercritical solvent. *AIChE J*. 1992;38:742–752.
63. Domingo C, Berends E, van Rosmalen GM. Precipitation of ultrafine organic crystals from the rapid expansion of supercritical solutions over a capillary and a frit nozzle. *J Supercrit Fluids*. 1997;10:39–55.
64. Li J, Matos HA, de Azevedo EG. Two-phase homogeneous model for particle formation from gas-saturated solution processes. *J Supercrit Fluids*. 2004;32:275–286.
65. Sparlart PR, Allmaras SR. A one-equation turbulence model for aerodynamic flows. *Recherche Aérospatiale*. 1994;1:5–21.
66. Pope SB. *Turbulent Flows*. Cambridge, UK: Cambridge University Press, 2000.
67. Tam CKW. Supersonic jet noise. *Annu Rev Fluid Mech*. 1995;27:17–43.
68. Panda J, Seasholtz RG. Measurement of shock structure and shock-vortex interaction in underexpanded jets using Rayleigh scattering. *Phys Fluids*. 2005;11:3761–3777.
69. Berland J, Bogey C, Bailly C. Numerical study of screech generation in a planar supersonic jet. *Phys Fluids*. 2007;19:075105.

Appendix A: Two-Dimensional Numerical Simulations of CO_2 Flow in the RESS/REHPS Device

The 1D model discussed in the main text is based on the assumption that average properties of CO_2, e.g., pressure, density, temperature, and velocity, do not vary rapidly in the direction of the mean flow, and the streamlines are nearly parallel. Additionally, a constant value was assumed for the friction factor in the momentum equation, as has been done in many studies.[40,43,44,53,62–64] In reality, however, the friction factor would depend on the flow rate, and thus, would be a function of position. Moreover, in the free expansion, the 1D flow approximation would not be applicable. To overcome these shortcomings, we carried out several 2D axisymmetric, steady-state CFD simulations using Fluent®. In these 2D simulations, as the friction occurs naturally through the interaction between the fluid and the wall, there is no need to specify the friction factor. Moreover, 2D simulations allow us to characterize the structure of the freely expanding jet and examine the role of the Mach disc in deagglomeration in more detail.

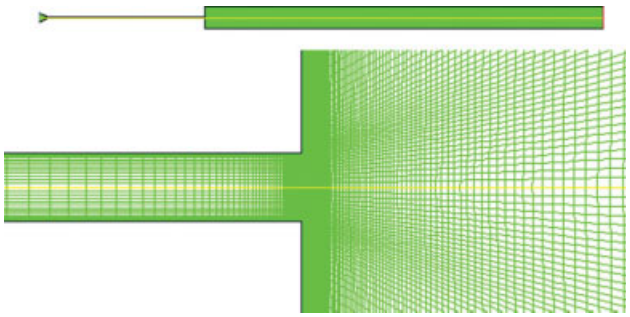

Figure A1. The axisymmetric RESS geometry used in the Fluent simulations. The mesh resolutions near the walls and near the exit of the nozzle are increased to capture the strong velocity gradients in those areas.

[Color figure can be viewed in the online issue, which is available at www.interscience.wiley.com.]

Figure A1 shows the computational mesh of the RESS device that includes a 5 mm converging section, a 102 mm long, 254 μm diameter nozzle, and a 300 mm long, 12.5 mm diameter tube. The mesh density was increased near the walls, near the inlet, and the exit to capture the rapid change in CO_2 properties in those regions (refer Figure A1 for an enlargement near the tip of the nozzle). Our simulations used the density-based solver option with second-order upwind scheme (available in Fluent), and applied constant-pressure boundary conditions at the inlet of the converging section (5.86, 3.45, and 2.07 MPa) and at the exit of the tube (0.1 MPa). As we limited our analysis to cases where

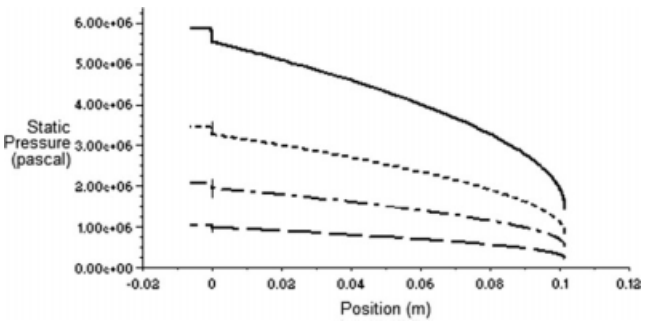

Figure A2. The variation of centerline pressure as a function of distance *x* from the inlet of the converging section (point 0) to the tip of the nozzle (point 2). P_0 = 5.86 MPa (solid line), 3.45 MPa (the long-dashed line), 2.07 MPa (the short-dashed line).

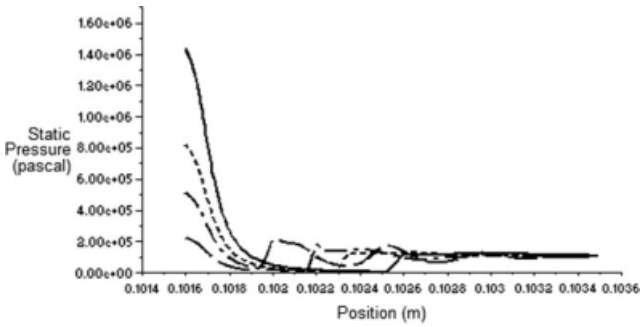

Figure A3. The variation of centerline pressure as a function of distance *x* from the tip of the nozzle (point 2) into the tube. P_0 = 5.86 MPa (solid line), 3.45 MPa (the long-dashed line), 2.07 MPa (the short-dashed line).

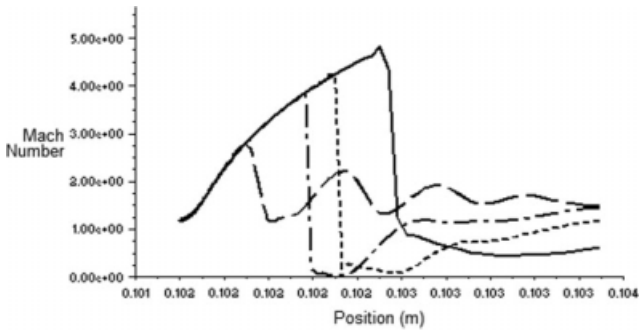

Figure A4. The variation of centerline Mach number as a function of distance *x* from the tip of the nozzle (point 2) into the tube. P_0 = 5.86 MPa (solid line), 3.45 MPa (the long-dashed line), 2.07 MPa (the short-dashed line).

condensation of CO_2 does not occur and as pressures are low in the free expansion, an ideal gas approximation was deemed sufficient. The Sparlart-Allmaras turbulent model (available in Fluent), a common choice for compressible flow simulations[65,66] was included.

Figure A2 shows the variation of the centerline pressure as a function of distance from the inlet of the converging section to the tip of the nozzle. The shapes of the profiles are very similar to that in Figure 13, indicating that the flow from point 0 to 2 can be described well by the 1D model even though it assumes a constant friction factor. P_2 obtained from Fluent simulations are very close to those obtained from 1D model calculations using the more accurate Span-Wagner EOS.[57]

Figure A3 shows the variation of centerline pressure as a function of distance away from the tip of the nozzle. For P_0 = 5.86 MPa, there is an abrupt increase in pressure about 0.64 mm (0.025 inch) away from the tip of the nozzle that is associated to a Mach disc. As the pressure after the abrupt change is only slightly higher than the atmospheric pressure

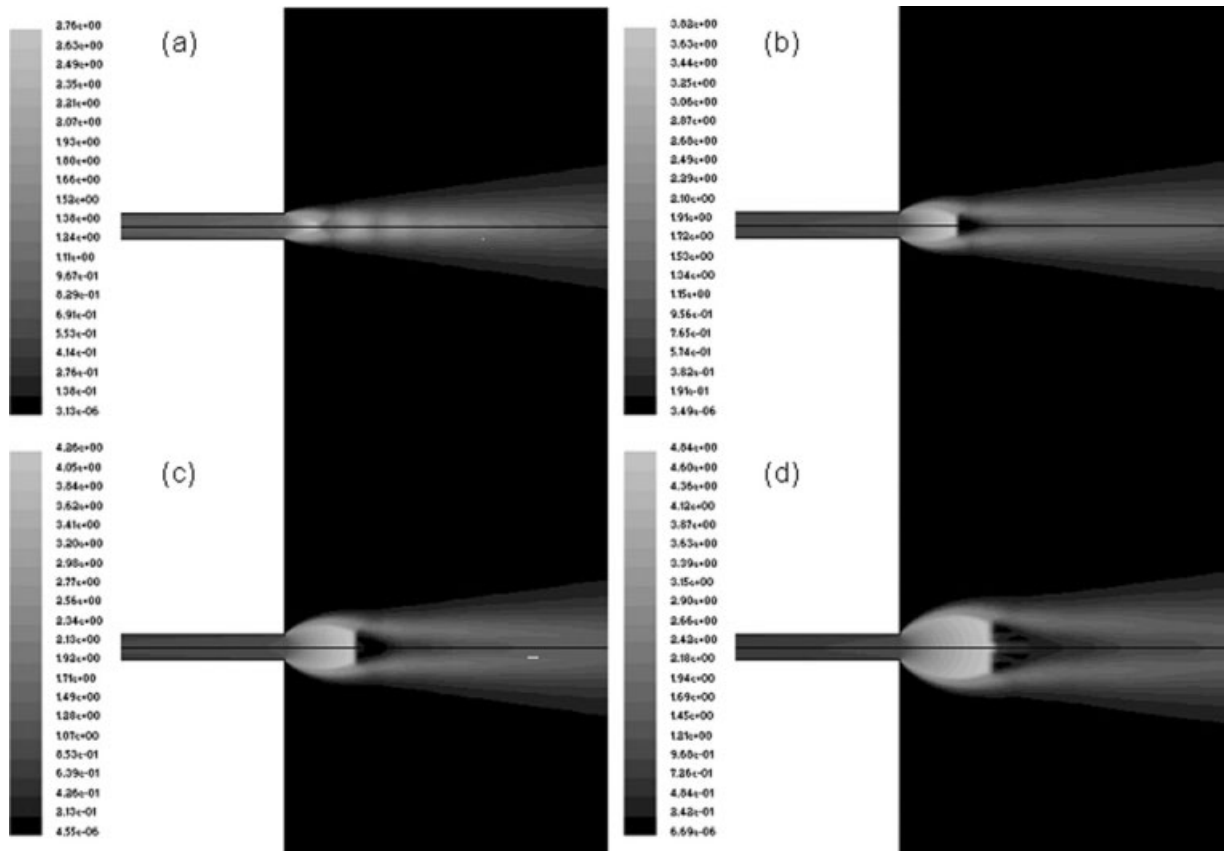

Figure A5. Mach number distribution near the exit of the nozzle. (a) P_0 = 1.03 MPa, (b) 2.07 MPa, (c) 3.45 MPa, and (d) 5.86 MPa.

0.1 MPa, it is reasonable in the 1D model to assume $P_4 \approx P_5 = 0.1$ MPa. As the pressure drops (3.45 MPa then 2.07 MPa), the abrupt change moves closer to the nozzle. For the lowest pressure 1.03 MPa, the abrupt change became more gradual, and there were fluctuations in the pressure that extended to about 2 mm away from the nozzle—they are pulses that are typical of a freely expanding supersonic jet when the pressure of the jet is not very high.[67–69]

The presence of a Mach disc is also evident in Figure A4 where we plot the centerline Mach number as a function of distance. The Mach number for the highest pressure 5.86 MPa reached 5, which is higher than the prediction of Eqs. 6–8. Again, at the lowest pressure, there were variations in the Mach number profile that suggest pulsating flow patterns.

Figure A5 contains three contour plots showing the Mach number distribution near the tip of the nozzle. It is clear that Mach discs were present at the three higher pressures $P_0 = 5.86$ MPa, 3.45 MPa, and 2.07 MPa. The size of the Mach disc decreases with decreasing pressure. As the inlet pressure was reduced to 1.03 MPa, the Mach disc disappeared and pulses started to form. Figure A5 also shows that, in the free expansion, not all material will pass through the Mach disc.

Manuscript received Aug. 11, 2008, and revision received Jan. 30, 2009.